Nanoscale Advances

Accepted Manuscript

This article can be cited before page numbers have been issued, to do this please use: S. K. Srivastava, M. Yadav, P. Singh, S. Tripathi, A. K. Verma and A. S. Parmar, *Nanoscale Adv.*, 2026, DOI: 10.1039/D5NA00964B.

ROYAL SOCIETY OF CHEMISTRY

rsc.li/nanoscale-advances

View Article Online
DOI: 10.1039/D5NA00964B

Biodegradable Folate-Mediated Chitosan-CQD Nanocarriers for Targeted and Stimuli-Responsive Cisplatin Delivery in Melanoma

Saurabh Kumar Srivastava[1,2], Monika Yadav[3#], Priyanka Singh[3#], Shikha Tripathi[1,2] Anita Kamra Verma[3,4*], Avanish Singh Parmar[1,2,5*]

[1]Biophysics and Nanotechnology Lab, Department of Physics, Indian Institute of Technology (BHU) 221005, Varanasi, India

[2]Proamyloidocare Pt. Ltd., Varanasi, Uttar Pradesh 221005, India

[3]Nano-Biotech Lab, Kirori Mal College, University of Delhi,110007, Delhi, India

[4]IoE Fellow, Delhi School of Public Health, Institution of Eminence, University of Delhi, Delhi 110007, India

[5]Centre for Biomaterials and Tissue Engineering, Indian Institute of Technology (BHU), Varanasi 221005, India

* *Corresponding authors:*

Email: asparmar.phy@itbhu.ac.in
akverma@kmc.du.ac.in

[#] *contributed equally*

View Article Online
DOI: 10.1039/D5NA00964B

ABSTRACT:

Polymeric nanoparticles provide an effective platform for drug delivery owing to their biocompatibility, biodegradability, and high drug-loading capacity. Chitosan, a natural cationic biopolymer, is particularly attractive because of its mucoadhesive nature, pH responsiveness, and structural stability. In this work, a cisplatin-loaded chitosan-based nanocarrier was developed by integrating green-synthesized fluorescent carbon quantum dots (CQDs) and surface functionalizing them with folic acid (FA) to enhance melanoma-targeted theranostic performance. Physicochemical characterization using UV–Vis spectroscopy, dynamic light scattering, and FTIR confirmed successful nanoparticle formation, surface functionalization, and colloidal stability, with a high cisplatin encapsulation efficiency (>70%). Hemocompatibility studies revealed negligible hemolysis, indicating excellent blood compatibility. The FA-conjugated cisplatin-loaded chitosan–CQD nanoconjugates (FA-CisCCNPs) exhibited significantly enhanced cytotoxicity against B16 melanoma cells, with markedly lower IC_{50} values compared to free cisplatin and non-drug-loaded FA–CCNPs. Fluorescence-based cellular internalization studies demonstrated efficient uptake of the nanoconjugates by melanoma cells, consistent with folate receptor-mediated endocytosis. In vivo studies in melanoma-bearing mice showed substantial tumor regression (approximately 70%), along with reduced systemic toxicity in vital organs and favorable modulation of oxidative stress biomarkers. Histopathological and immunohistochemical analyses further associated tumor suppression with p53 overexpression and Bcl-2 downregulation, supporting the potential of FA-CisCCNPs as a green-synthesized, biodegradable, and stimuli-responsive nanoplatform for targeted melanoma therapy.

Keywords: Carbon quantum dots, Chitosan nanoparticles, Melanoma, targeted delivery, folate-conjugated nanoparticles, cytotoxicity

Aberration used:

CQDs- Carbon quantum dots

CCNPs- chitosan carbon quantum dots nanoparticles

FA-CCNPs – Foilc acid tagged chitosan carbon quantum dots nanoparticles

FA-CisCCNPs - Foilc acid tagged Cisplatin loaded chitosan carbon quantum dots nanoparticles

Cis - Cisplatin

View Article Online
DOI: 10.1039/D5NA00964B

H/E- Histological stain (hematoxylin/eosin)

IHC- immunohistochemical

SF- Supplymentry file

1. Introduction:

Melanoma is a highly aggressive and malignant form of skin cancer that originates from melanocytes, the melanin-producing cells primarily located in the basal layer of the epidermis [1]. Although melanoma accounts for only a small proportion of total skin cancer cases (approximately 4%), it is responsible for nearly 75% of skin cancer-related deaths worldwide [2] [3]. Its rapid progression, strong metastatic potential, and frequent recurrence contribute to poor clinical outcomes. Despite recent advances in immunotherapies and molecularly targeted treatments, melanoma remains challenging to treat due to therapy-associated toxicity, high treatment costs, incomplete tumor eradication, and the emergence of drug resistance [4]. These limitations necessitate the development of alternative therapeutic strategies that improve tumor selectivity and treatment efficacy while minimizing systemic adverse effects.

Cisplatin (Cis), the first platinum-based chemotherapeutic agent approved by the U.S. Food and Drug Administration, remains a clinically relevant anticancer drug and is widely used in melanoma management[5]. Its mechanism of action involves the formation of DNA crosslinks that inhibit DNA replication and transcription, ultimately inducing apoptosis in rapidly proliferating tumor cells [6]. However, the clinical use of cisplatin is significantly limited by its poor pharmacokinetic profile, off-target accumulation, nephrotoxicity, neurotoxicity, and gastrointestinal toxicity. In addition, the development of intrinsic or acquired drug resistance mediated by enhanced DNA repair mechanisms, increased drug efflux, and intracellular detoxification further reduces its therapeutic effectiveness[7,8].These challenges highlight the urgent need for improved cisplatin delivery systems that enhance tumor accumulation and reduce systemic toxicity.

Nanotechnology-based drug delivery systems have emerged as promising approaches to overcome these limitations[9]. Encapsulation of cisplatin within biocompatible nanocarriers, including polymeric nanoparticles, liposomes, and micelles, has been shown to improve drug stability, prolong circulation time, enable controlled release, and facilitate receptor-mediated endocytosis[10] [11].Such nanocarriers enhance tumor accumulation via both passive and active targeting mechanisms, thereby improving therapeutic efficacy while minimizing damage to healthy tissues

View Article Online
DOI: 10.1039/D5NA00964B

[12]. Among various polymeric materials, chitosan has attracted considerable interest as a drug delivery vehicle due to its favourable physicochemical and biological properties.

Chitosan is a naturally derived, cationic polysaccharide obtained through the deacetylation of chitin and is known for its biocompatibility, biodegradability, low toxicity, and mucoadhesive nature[13] [14]. The presence of positively charged amino groups allows chitosan to interact electrostatically with negatively charged drugs and biomolecules, facilitating efficient drug encapsulation and controlled release[15], Moreover, chitosan can be readily formulated into nanoparticles or hydrogels under mild conditions, making it suitable for biomedical applications. Its pH-responsive behaviour enables preferential drug release in the mildly acidic tumor microenvironment, thereby enhancing drug bioavailability and therapeutic efficacy[16] allows chitosan-based carriers to preferentially dissolve and release their payloads in the mildly acidic tumor microenvironment, thereby enhancing drug bioavailability and therapeutic efficacy. These properties collectively make chitosan a highly suitable and versatile vehicle for targeted drug delivery for cancer therapy [17].

Targeted drug delivery can be further improved by functionalizing chitosan nanoparticles with ligands such as folic acid, which selectively binds to folate receptors overexpressed on the surface of many cancer cells, including melanoma[18]. Folate receptors, particularly FRα and FRβ, are highly expressed in tumor tissues but show minimal expression in most normal cells [19]. Folic acid-functionalized nanoparticles therefore enhance cellular uptake through receptor-mediated endocytosis, improve tumor-specific drug accumulation, and reduce off-target toxicity[20]. While folate-mediated targeting has been explored in cisplatin delivery systems, most reported formulations lack integrated imaging capability, limiting their potential for real-time monitoring and theranostic applications.

Carbon quantum dots (CQDs) are fluorescent, carbon-based nanomaterials characterized by excellent biocompatibility, low toxicity, tunable photoluminescence, and high aqueous solubility [21,22,23]. Their small size and abundant surface functional groups enable strong interactions with biological systems, making them suitable for biomedical imaging and drug delivery applications. When combined with chitosan, CQDs form multifunctional nanocomposites that offer enhanced structural stability, controlled drug release, and fluorescence-based bioimaging capabilities[24]. However, the combined use of CQD-based imaging and folate-mediated targeting within cisplatin-loaded chitosan nanocarriers remains relatively unexplored.

View Article Online
DOI: 10.1039/D5NA00964B

In this study, we address this gap by developing fluorescent, folate-conjugated, cisplatin-loaded chitosan-carbon quantum dot nanoparticles (FA-CisCCNPs) using an ion gelation method. This nanoplatform integrates active folate-receptor[25] targeting with CQD-based fluorescence for simultaneous therapeutic delivery and imaging. The FA-CisCCNPs demonstrated enhanced biocompatibility, selective cytotoxicity against B16 melanoma cells, efficient cellular internalization, and pH-responsive controlled drug release. These findings support the potential of FA-CisCCNPs as a multifunctional and targeted nanoplatform for melanoma therapy with theranostic capability.

2 Materials and methods

2.1 Materials:

Triton-X, 5,5′-Dithiobis (2-nitrobenzoic acid) (DTNB), 1-Chloro-2,4-dinitrobenzene (CDNB), 5,5′-Dithiobis (2-nitrobenzoic acid) (HEPES), 5,5′-Dithiobis (2-nitrobenzoic acid) (DTNB), and Dimethyl sulphoxide (DMSO)—were bought from Sigma-Aldrich (USA). We bought β-nicotinamide adenine dinucleotide phosphate (NADPH), glutathione reductase (GR), and oxidized glutathione (GSSG) from MP Biomedicals in India. We bought Trichloroacetic acid (TCA), Sodium pyrophosphate, Nitroblue tetrazolium (NBT), nicotinamide adenine dinucleotide (NADH), sulphanilamide, N-1-nepthylethyldiamine dihydrochloride (NEDD), ortho-phosphoric acid, Tris-HCl, Ethanol, Sodium pyuruvate, Sodium chloride, Ethylene diamine tetra-acetic acid (EDTA), and other chemicals from SRL in India. All of the tests used water that has been double-distilled and deionized. Cisplatin (cis-diamine platinum (II) dichloride), tripolyphosphate, RPMI-1640 medium, fetal bovine serum, and medium molecular weight chitosan (75% degree of deacetylation, 200–300 cP viscosity grade) were all bought from Sigma in the USA.

2.2 Methodology

2.2.1 Preparation of Carbon Quantum Dots (CQDs)

Firstly, the carbon quantum dots (CQDs) was synthesised by previously reported green hydrothermal methods[26] . The Mahogany (Swietenia macrophylla) leaves plant extract was placed in

View Article Online
DOI: 10.1039/D5NA00964B

a 200 mL stainless steel autoclave chamber and heated to 160 °C for eight hours in a muffle furnace. After hydrothermal treatment, a solution with a dark brown color was obtained. Following that, the supernatant was obtained by centrifuging at 10,000 rpm for 15 minutes at 27 °C. The larger particles were removed from this supernatant by filtering it through a 0.2 μm syringe filter. Filtered CQDs were subsequently collected and stored at 4 °C. The yield amount of filtered CQDs was 8mg/ml.

2.2.2 Preparation of chitosan-CQD nanoparticles (CCNPs)

Chitosan is a natural polymer that is poly-cationic, while tripolyphosphate (TPP), which was used as a cross-linker, is an anionic substance. Chitosan and TPP were able to bond with ions by attracting each other. At first, glacial acetic acid was mixed with 0.5% chitosan polymer by weight. CCNPs were prepared using the ionic gelation method[27]. Then, the pH was adjusted to 4.6 ± 0.2 using 10 N sodium hydroxide (NaOH). 0.5% (w/v) tripolyphosphate and the solution was clarified by heating on a hot plate at 60 °C stirred for 10 min with a magnetic bead. Additionally, 100 μL of CQDs (1% v/v) was mixed dropwise into the solution. Following this, the TPP solution was added dropwise at a 1:4 volume ratio (TPP:chitosan) at a controlled rate of 0.5 mL/min while maintaining magnetic stirring on a hot plate. Nanoparticle formation was instantaneously initiated upon TPP addition and further enhanced by probe sonication to ensure uniform size distribution and minimize aggregation. The resultant CCNPs were collected by centrifugation at 10,000 rpm for 30 min at 4 °C, the supernatant was discarded, and then the NPs were redispersed in distilled water.

2.2.3 Preparation of FA tagged chitosan-CQDs nanoparticles (FA-CCNPs)

The folic acid (FA) functionalization of chitosan-CQD nanoparticles (CCNPs) was performed via a carbodiimide-mediated coupling reaction, adapted from established protocols with slight modifications[28]. 64 mg of folic acid (FA), equimolar NHS (FA:NHS = 1:1), and twice molar excess of EDC (FA:EDC = 1:2) were dissolved in a mixture of 20 mL dry dimethyl sulfoxide (DMSO) and 40 mL deionized (DI) water under constant stirring. This solution was added dropwise to a pre-prepared dispersion of CCNPs under gentle stirring to promote homogeneous conjugation. The reaction was allowed to proceed for 16 hours in the dark at 30 °C. The mixture was purified through dialysis in phosphate buffer of pH = 7.4 for 3 days and then in double-distilled water for 3 more days. Its isolation was done through freeze-drying method and the final yield for 60ml of reaction was approximate 1gram.

View Article Online
DOI: 10.1039/D5NA00964B

2.2.4 Preparation of FA tagged cisplatin-loaded chitosan-Carbon quantum dot nanoparticles (FA-CisCCNPs)

FA-CisCCNPs were formulated using an ionic gelation technique. During the preparation of FA-CCNPs, cisplatin (0.05%, w/v), CQDs (1% v/v), and 0.5% (w/v) TPP were added to the chitosan solution, mixed using a laboratory probe sonicator. Sonication occurred at 15-minute intervals for 3 minutes at 100% amplification during mixing. After 90 min of stirring, the product was eluted and refrigerated at 2–8 °C.The reaction was purified through dialysis in phosphate buffer of pH = 7.4 for 3 days and then in double distilled water for 3 more days. Its isolation was done through freeze-drying. As a result, a yellowish product was obtained. FA-CCNPs & FA-CisCCNPs were washed 3-4 times in a centrifuge tube at 10,000 rpm with DI water for the removal of excess amount of DMSO and Acetic acid for the use of in-vitro/in-vivo experiments. This was further lyophilized and kept at 4.0 °C until used in the subsequent study.

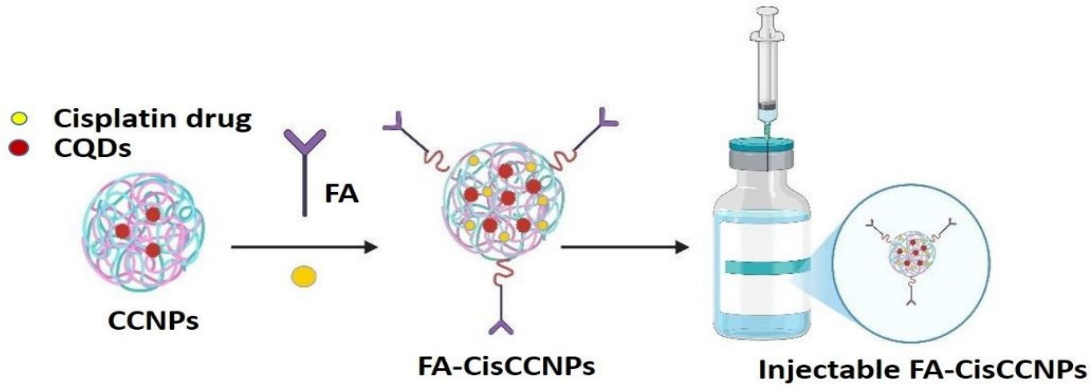

Schematic diagram of preparation of injectable FA-CisCCNPs

2.3 Physicochemical characterization of nanoparticles.

Synthesized nanoformulation was prepared for physicochemical characterization. Briefly, 1% (w/v) solution of each formulation (FA-CisCCNPs and FA-CCNPs) was prepared in 1% DW solution, and a uniform colloidal solution of the formulation was generated by the sonication method. The synthesized nanoparticles were characterized for their size and zeta potential using dynamic light scattering (DLS) (ELSZ2; Photal Otsuka Electronics, Osaka, Japan), using the cumulant method and histogram method. Fluorolog-Horiba fluorescence spectrophotometer, the PL emission spectra were recorded (HORIBA Jobin Yvon, France) to determine the fluorescence

View Article Online
DOI: 10.1039/D5NA00964B

of CQDs in FA-CisCCNPs. The thermogravimetric analysis of the conjugate and nanoparticles was accomplished by means of a Mettler Toledo TGA/SDTA 851 system for monitoring mass losses in the destructive process as the temperature increases. Structural properties were assessed with FTIR The new bindings formed in the chitosan derivatives, as well as between the crosslinking agents and the modified polymer in the formation of nanoparticles, were evidenced using two spectrometers BONEM 108B, Canada, and DIGILAB Scimitar FTS 200, USA by the KBr pellet technique. X-Ray Diffractometer (XRD, Rigaku Ultima IV), operated at 20 kV, 20 mA with Cu-Kα radiation (λ=1.5405 Å) in the 2θ range of 40° to 120°. For morphological characterizations, Field emission scanning electron microscope (FESEM, ZEISS Gemini SEM 500) operated at 10 kV and Transmission electron microscope (TEM, FEI TECNAI G2 20 TWIN USA) operated at 200 kV were used. Elemental analysis was done using an energy dispersive X-ray spectrometer (Rigaku Miniflex 600 Desktop X-Ray Diffraction System, Tokyo, Japan) attached to the FE-SEM.

2.4. Encapsulation efficiency.

Entrapped cisplatin was determined in 5 mg of each lyophilized formulation (FA-CisCCNPs and FA-CCNPs) by suspending it in 10 mL of DW solution in a flask kept on magnetic stirring for 30 min[29]. The reaction mixture was centrifuged at 2000 rpm and the supernatant was kept at 2 °C. The concentration of cisplatin was extrapolated from the cisplatin standard calibration curve, by using UV-VIS spectroscopy at absorbance peak of 207nm. the calibration curve equation is y = 0.0003x + 0.0025, R^2= 0.9897 value mentioned in FigS1. Then, the encapsulation efficiency% (EE) and drug loading (DL)% were calculated using the following equations:

$$EE(\%) = \frac{Amount\ of\ drug\ incorporated - amount\ of\ free\ drug\ after\ extraction}{Amount\ of\ drug\ incorporated} \times 100 \ldots\ldots (1)$$

$$DL(\%) = \frac{Total\ amount\ of\ drug\ incorporated\ in\ nanoparticles}{Total\ weight\ of\ nanoparticles} \times 100 \ldots\ldots\ldots\ldots (2)$$

2.5. In vitro release study.

Dialysis bag (DB) release tests on FA-CisCCNPs and FA-CCNPs were done in triplicate. 5 mg of each lyophilized formulation of FA-CisCCNPs and FA-CCNPs was placed in a DB and immersed separately in 50 mL of phosphate buffer saline, pH 5.8 & pH 7.4, at 37 °C with a magnetic bead stirring at 1000 rpm for 72 hr. First sampling was 30 minutes to assess release. Next, 3 mL of

View Article Online
DOI: 10.1039/D5NA00964B

medium was removed every 1 hr and replaced with fresh medium. Using UV/visible spectroscopy at the absorbance peak of 207nm, the release pattern was identified by drawing a graph OD of cisplatin concentration against time[30]. Details of the drug release kinetic model are described in supplementary files section SFS1.

2. 6 In vitro studies

2.6.1 In vitro cytotoxicity study.

The cytotoxicity of the FA-CisCCNPs, FA-CCNPs, and free Cis at concentrations of 62.5, 125, 250, 500 and 1000 µg/mL and equivalent Cis was evaluated and the percent cytotoxicity was calculated in B-16 cell line[31]. Briefly, 5x10^3 cells/well were seeded in a 96-well microliter plate, supplemented with 10% FBS, followed by incubation for 24 hr at 37°C with an atmosphere of 5% CO_2. Subsequently, the medium was replaced with fresh medium containing various concentrations of the test formulations, and the cells were exposed for 24 hr and 48 hr. After the requisite time period, 20 µL of MTT solution (5 mg/mL in PBS pH 7.4) was added to each well, and the plates were incubated at 37 °C for 4 hr, allowing the formation of formazan crystals that were further dissolved in 150 µL of DMSO. The absorbance was recorded at 570 nm using a microplate reader (Synergy HT, BioTek, USA) after brief mixing on a mechanical plate shaker.All experiments were conducted in triplicates, and data were presented as mean ± standard deviation. The absorbance measured was directly proportional to the number of viable cells. The percent (%) cytotoxicity was calculated using described formula:

$$\%\ \text{cytotoxicity} = \frac{[A]control - [A]test}{[A]control} \times 100 \ldots\ldots\ldots\ldots\ldots\ldots\ldots\ldots\ldots\ldots\ldots\ldots \quad (3)$$

Where, $[A]_{test}$ = Absorbance of the sample to be test

$[A]_{control}$ = Absorbance of the control sample

2.6.2 In-vitro cellular uptake study.

B-16 (50,000 cells/ well) were inoculated on 12mm round glass cover slip in a 24 well microplate in complete growth media. After 24 hours, the media and cells were treated with FA-CCNPs for 2 hr and 4 hours. Following incubation, the medium was aspirated, and the cells were washed twice with chilled PBS. The cells were then fixed with 4% paraformaldehyde for 30 min. After fixation, cells were again washed with PBS to eliminate any residual fixative and DAPI (1µg/mL) was added to the treated cells to mark the nucleus. Again, Excess stain was removed by washing twice

View Article Online
DOI: 10.1039/D5NA00964B

with chilled PBS. Cover slips were mounted in DPX on the slides and were visualized under a confocal microscope.

2.6.3 Ex-vivo Hemolysis Assay

Mice blood was taken in EDTA tubes to test FA-CisCCNPs, FA-CCNPs, and Cis for hemolysis. Whole blood was added to an equal volume of PBS at pH 7.4, centrifuged at 1500 rpm for 5 min, and plasma was discarded. After centrifugation, blood cells were washed again with PBS (7.4) and the supernatant discarded. Equal volumes of cleansed red blood cells were added to PBS (7.4). . 200 µL of these cells were taken in each micro-centrifuge tube and FA-CisCCNPs, FA-CCNPs and Cis were added. All the micro centrifuge tubes were kept at room temperature, under continuous stirring on a shaker for 2 hr and 4 hr. After 2 and 4 hours of incubation, the tubes were centrifuged at 11,000 rpm for 5 min, the supernatant was transferred to a 96-well plate, and absorbance was recorded at 540 nm. Positive control was Triton –X (0.1%) while negative control was PBS pH 7.4[32]. Percent hemolysis was calculated by the formula:

$$\%\ \text{Hemolysis} = \frac{(\text{Abs})\ \text{sample} - (\text{Abs})\text{saline}}{(\text{Abs})\ \text{positive control} - (\text{Abs})\text{saline}} * 100 \ldots\ldots\ldots(4)$$

2. 7 In-vivo studies

The in-vivo experiments were carried out in accordance with the animal Ethical Committee of University of Delhi, India under registration number 1666/GO/Re/S/12/CPCSEA; Protocol number (DU/KR/IAEC/2023/13B). 6-8 week old female C57 BL/6 mice will be initially housed in plastic cages with a 12 hr/12 hr light–dark cycle at 22 °C-24 °C temperature, 40-60% humidity and free access to food and water[33].

2.7.1 Tumor regression study

After being acclimatized to laboratory conditions, animals weighing 20g ± 5.00g at the beginning of the experiment were inoculated subcutaneously with 2×10^6 B16-F10 cells in 100 μL per site on the dorsolateral aspect of the mice. After 5-7 days, when the tumor size reached 100 mm^3 of volume, C57BL/6 mice were randomly allocated to 4 groups with three animals in each group. Group 1 was control (tumor mice, untreated), receiving intravenous injection (alternative days) of only saline; Group 2, FA-CCNPs; Group 3, cisplatin and Group 4, FA-CisCCNPs were given a

View Article Online
DOI: 10.1039/D5NA00964B

dose of (3mg/kg) intravenous injection on alternate days for 21 days. For 21 days, the tumor volume and body weight of the mice were recorded on alternate days, and after 21 days, the animals were sacrificed, and organs were harvested and used for oxidative analysis, estimating the levels of LDH, NO, GSH, GST, and SOD. Further organs were preserved in 10% formalin solution for histology[34] and IHC studies[35]. The detailed experimental procedure for biochemical assay, histology and IHC has been described in the SF section S2&S3. The formula used to determine the tumor volume:

$$\text{Tumor Volume} = (\text{Length} \times \text{Width}^2)/2 \quad \ldots\ldots\ldots\

View Article Online
DOI: 10.1039/D5NA00964B

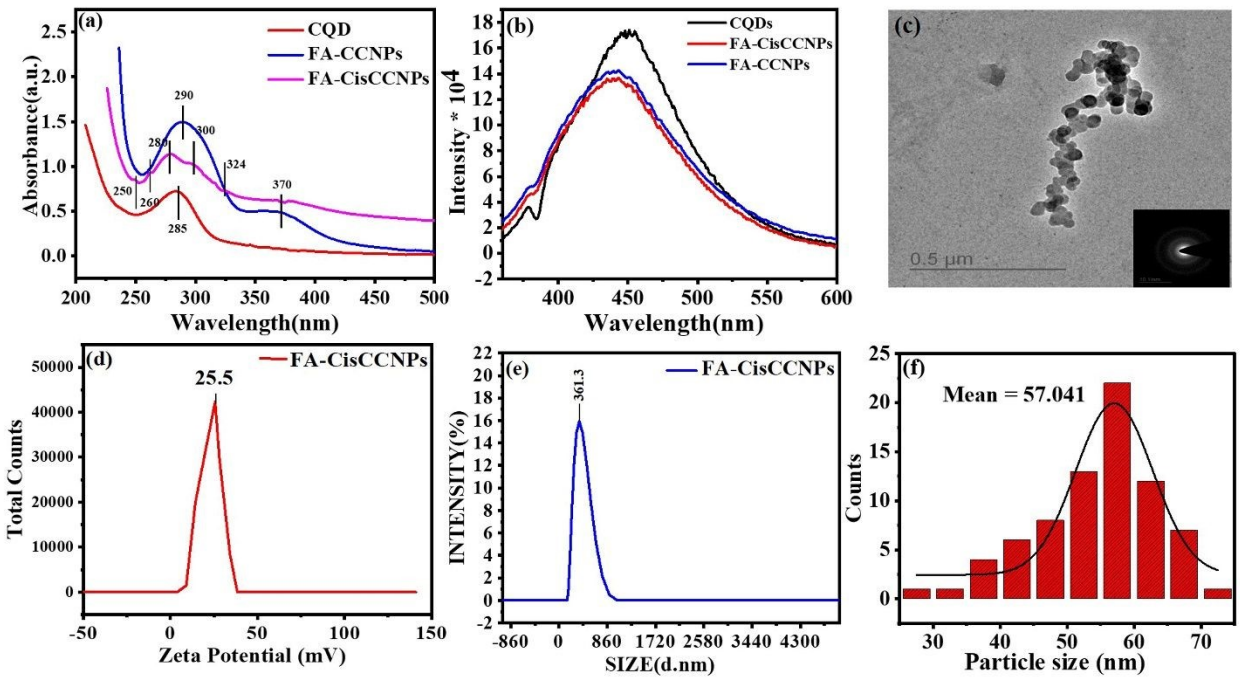

Fig 1(a) Uv-Vis spectra of CQDs, FA-CCNPs and FA-CisCCNPs (b) PL emission spectra of CQDs, FA-CCNPs and FA-CisCCNPs (c) Tem image of FA-CisCCNPs (d,e) Zeta potential and DLS measurement of FA-CisCCNPs (f) size distribution bar graph plot of FA-CisCCNPs

The optical properties and molecular interactions of the synthesized CQDs, FA-CCNPs and FA-CisCCNPs were examined using UV–Vis spectroscopy Fig1(a). The formation of conjugated graphitic domains was confirmed by the strong absorption peak in the UV spectrum, for CQDs at 285 nm, which is associated with the π–π* electronic transitions of aromatic C=C bonds in the sp^2-hybridized carbon core[36]. Because of the n–π* transitions of non-bonding electrons on nitrogen atoms (from NH_2 groups), FA-CCNPs showed a distinctive broad absorption peak at about 290-320 nm, indicating the presence of free amino functionalities and the structural integrity of chitosan[37]. Following their functionalization with folic acid and CQDs, the FA-CCNPs showed a red-shifted absorption peak at about 370 nm. This was linked to electronic interactions between CQDs and chitosan as well as π–π* transitions in the aromatic rings of folic acid[38], suggesting that surface modification and conjugation had been successful[39]. Folate tagging on the surface of the nanoparticles is confirmed by the absorbance in this area. Additional absorption peaks with slight

View Article Online
DOI: 10.1039/D5NA00964B

shifts in relation to precursor components emerged at 300 and 362 nm for the cisplatin-loaded system (FA-CisCCNPs)[40]. These peaks, which confirm successful cisplatin loading onto the nanoparticles matrix, are ascribed to ligand-to-metal charge transfer (LMCT) transitions of the platinum moiety. The presence and integration of CQDs, chitosan, folic acid, and cisplatin within a single nanocomposite system are confirmed by above mentioned peaks[41].control UV-Vis absorption spectra of Chitosan, FA and Cis added in the supplementary file Fig S1 (b) for comparative analysis. Additionally, the spectrum displays wider absorption tails, indicating improved electronic coupling and the possibility of light-responsive biomedical uses like bioimaging or photodynamic therapy.

Fig1 (b) shows the PL Fluorescence behaviour of the CQDs alone and FA-CisCCNPs in aqueous solution, with 340 nm excitation wavelength. As reported by Srivastava et al carbon quantum dots exhibit excellent photostability and long-term fluorescence retention, showing negligible loss in photoluminescence intensity under continuous UV irradiation, across a broad pH range, and even after prolonged storage, which supports their suitability for reliable and sustained bioimaging applications. The CQDs demonstrated maximum fluorescence intensity at 440 nm, while in the case of FA-CCNPs and FA-CisCCNPs, its PL fluorescence intensity gets reduced. FA-CisCCNPs show slightly reduction in the PL fluorescence intensity as compare to the FA-CCNPs due to masking of CQDs as cisplatin were added into the formulation. The reduction in the fluorescence intensity does not affect the bioimaging property of CQDs. Further ZP of the FA-CisCCNPs was determined to be +25.5 mV, indicating the highly cationic and stable nature of the nanoparticles Fig1(d). An earlier study reported that the ZP of chitosan solution ranged from +1.65 to +42.8 mV[42]. DLS size of FA-CCNPs was measured to be 335nm shown in FigS1(c). Fig1(e) shows the mean hydrodynamic size of the FA-CisCCNPs was measured to be 361.3nm with poly dispersity index of 0.257±0.030, increase in DLS size before and after drug loading confirms the successful cisplatin drug loading and homogeneity as well. TEM analysis Fig1(c) showed that the

View Article Online
DOI: 10.1039/D5NA00964B

morphology of FA-CisCCNPs nanoparticles cross-linked with TPP was spherical and smooth with average particle sizes 57.04 nm and having mono dispersed nature Fig1(f)[43].

Fig 2(a) FTIR spectra of CQD, FA, FA-CCNPs & FA-CisCCNPs (b) X-RD peak of Cisplatin drug (Cis), FA-CCNPs & FA-CisCCNPs (c) TGA plot of Cisplatin drug (Cis), FA-CCNPs & FA-CisCCNPs (d,e) SEM image of FA-CCNPs & FA-CisCCNPs

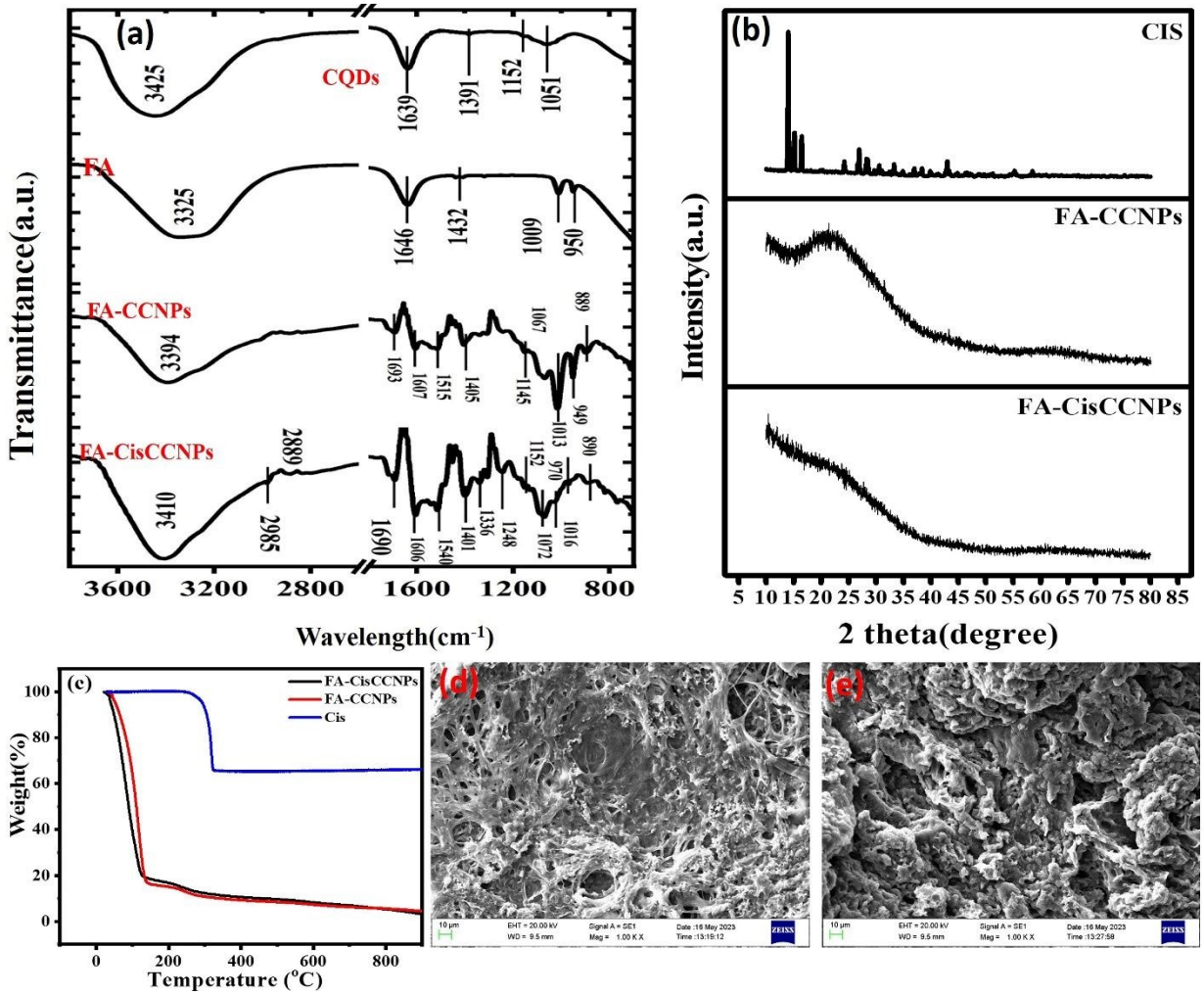

FTIR spectrum of CQDs Fig2(a) shows a broad absorption band at 3425 cm^{-1}, corresponding to overlapping O-H and N-H stretching vibrations, indicating the presence of hydroxyl and amine surface groups. A weak C–H stretching is observed around 2985 cm^{-1}. CQDs also confirm the presence of the peak at 1639 cm^{-1} arises from carbonyl (C=O) stretching of surface-bound carboxylic groups, while peaks around 1639 cm^{-1} and 1391 cm^{-1} indicate N–H bending and C–N

View Article Online
DOI: 10.1039/D5NA00964B

stretching, respectively. Peaks at 1051 cm^{-1} are attributed to C–O or O–CO vibrations, confirming surface oxygenated functionalities that impart hydrophilicity and fluorescence[44]. The FTIR spectrum of the major peaks of the pure molecules such as Chitosan and Cisplatin are defined from previously reported literature [45 46 47] . The FTIR spectrum of folic acid displays characteristic bands at 3325 cm^{-1} for O–H/N–H stretching, and 1646 cm^{-1} for C=O stretching of carboxyl and amide groups. Additional bands at 1432 cm^{-1} (CH_2 bending) and 1009 cm^{-1} (C–O stretching) confirm its polyfunctional aromatic structure. These peaks serve as markers for successful conjugation with chitosan polymers. The spectrum of chitosan nanoparticles, pre-loaded with CQDs and functionalized with folic acid, shows cumulative peaks from all components, confirming successful hybrid formation. The broad band at 3394 cm^{-1} arises from O–H and N–H stretching from both chitosan and folic acid. Peaks at 2889 cm^{-1} represent C–H asymmetric stretching (CH_3/CH_2). The amide I peak at 1607 cm^{-1} (C=O stretching) and 1432 cm^{-1} (CH_3 bending) originate from chitosan's residual acetylated groups and folic acid's aromatic system. The peak at 1009 cm^{-1}, along with minor shoulders around 950–950 cm^{-1}, corresponds to the C–O–C stretching of the polysaccharide backbone and CQDs surface groups[48]. Integration of CQDs is evident by the preserved C–N/C–O–C peaks in the 1000–1070 cm^{-1} region, while the folic acid signature is reflected by broadening of the aromatic region (1400–1600 cm^{-1}). This hybrid spectrum suggests successful embedding of CQDs and functionalization of FA into the chitosan nanoparticles matrix without significant structural degradation. The final nanocomposite spectrum displays overlapping but shifted and intensified peaks, indicating successful Cisplatin drug loading and enhanced molecular interactions. The broad O–H/N–H stretch shifts slightly higher to 3410 cm^{-1}, with increased intensity, suggesting hydrogen bonding and coordination with cisplatin. The CH_2 peak at 2985 cm^{-1} remains present, confirming structural integrity. A distinct amide I band appears at 1606 cm^{-1},1690 cm^{-1}, indicating strong interaction between cisplatin and chitosan or FA amino groups. Peaks at 1401 cm^{-1} represent CH_3 bending, with slight shifts compared to their counterparts in individual materials, further suggesting conjugation and complexation. Importantly, a new band at 1051 cm^{-1} appears, corresponding to P–O stretching, attributed to cisplatin incorporation. The C–O–C asymmetric stretching of chitosan and CQDs remains around 1016 cm^{-1}, though slightly broader, confirming matrix preservation with drug incorporation. FTIR analysis clearly demonstrates the successful stepwise integration of CQDs, folic acid, chitosan, and cisplatin in the nanocomposite. Shifts in key peaks and intensity changes confirm molecular

View Article Online
DOI: 10.1039/D5NA00964B

interactions, chemical binding, and structural compatibility. The presence of characteristic functional groups from all individual components in the final spectrum validates the effective synthesis of a targeted FA-CisCCNPs.

X-ray diffraction (XRD) analysis was carried out to investigate the structural characteristics and confirm the successful formulation of the synthesized FA-CisCCNPs Fig2(b). The pure cisplatin exhibited sharp and intense diffraction peaks at 14.06°,17.10°,37.70°,64.30°, confirming its highly crystalline nature due to the well-ordered arrangement of platinum-containing molecules[49]. In contrast, FA-CCNPs displayed a broad amorphous halo centered around 24° & 60° (2θ)[50], indicating a non-crystalline, polymeric matrix structure. This amorphous nature is attributed to the molecular dispersion of folic acid and CQDs within the chitosan backbone. Upon encapsulation of cisplatin, the resulting FA-CisCCNPs exhibited a change in the intensity & shifting at peak 24° (2θ), along with peaks at 37°, 62°. The characteristic peaks of cisplatin were reduced in intensity and broadened, implying that the drug was successfully encapsulated in a less ordered form. The shift and changes in peak positions are indicative of interactions between the FA-CisCCNPs, leading to complex formation. These findings confirm the successful incorporation of cisplatin into the FA-CCNPs.

Thermogravimetric analysis of Cis, FA-CCNPs, and FA-CisCCNPs shown in Fig 2(c). From the plot it is visible that Cisplatin exhibited relatively high mass retention up to 400 °C, which can be attributed to its inorganic platinum content and lower proportion of volatile organic components. In contrast, both FA-CCNPs and FA-CisCCNPs showed pronounced mass loss below 200 °C. This early weight loss is not solely due to residual moisture, as the samples were lyophilized, but is more reasonably associated with the decomposition of low-molecular-weight species[51] and thermally labile functional groups present in the chitosan-based formulations[52]. The main degradation step for FA-CCNPs and FA-CisCCNPs occurred between 200 and 400 °C, corresponding to the thermal breakdown of the chitosan backbone[53]. FA-CisCCNPs displayed a slightly higher residual mass at elevated temperatures compared to FA-CCNPs, which is likely related to the presence of platinum from cisplatin rather than a significant enhancement in intrinsic polymer thermal stability. The TGA results primarily reflect compositional differences among the samples and confirm successful cisplatin incorporation into nanoparticle.

View Article Online
DOI: 10.1039/D5NA00964B

Fig2(d,e) shows the SEM images of bulk lyophilized powder of synthesised FA-CCNPs & FA-CisCCNPs formulations. Chitosan-based nanoparticles are known to retain a fraction of bound or strongly hydrogen-bonded water due to the abundance of hydroxyl and amino groups within the polymer matrix[54]. The porous and interconnected matrix network observed in SEM images arises from polymer chain fusion and hydrogen bonding during the lyophilisation process[55], which is a well-known behaviour for chitosan-based nanoparticle systems. The interconnected network structure of the FA-CCNPs suggests a large surface area that is good for drug loading applications. On the other hand, FA-CisCCNPs exhibit a more compact and dense interconnected network structure, probably due to the cisplatin encapsulation which causes structural rearrangement, reduced pore size, and dense structure. This modification shows the effective loading of cisplatin[56]. This bulk morphology does not represent individual nanoparticles but rather the solid-state organization of the dried formulation. FigST2 confirms the presence of various elements such as carbon, nitrogen, oxygen, sulphur in FA-CCNPs & FA-CisCCNPs formulations. Presence of additional element as platinum (Pt) and chlorine (Cl) confirms that the anti-cancer drug Cisplatin has been successfully encapsulated in FA-CisCCNPs.

3.2 Encapsulation efficiency and release kinetic studies

The EE% and DL% was 60% ± 1.54 and 6% ± 0.98 and %, respectively. These results corroborate the findings of previous studies[57]. The continued release of the drug from the nanoparticles was analysed using various mathematical models[41] FigS2(a-d). To properly understand the effectiveness of the drug delivery system, it was crucial to consider both the target distribution pattern and the mechanism by which the drug is released. The findings demonstrated that at both pH 7.4 and pH 5.8, the release of Cis from FA-CisCCNPs exhibited a first-order kinetic pattern. An initial rapid burst release was observed, which was subsequently followed by a controlled, sustained release over a period of 72 hours with R^2 value as 0.2007 and 0.2108 at pH 7.4 and 5.8, respectively.

3.3 In vitro studies

3.3.1 % cytotoxicity evaluation for B-16 cell line

View Article Online
DOI: 10.1039/D5NA00964B

In this study, the inhibitory effects of FA-CCNPs & FA-CisCCNPs and Cis (Cisplatin) on the growth of B-16 cells were evaluated based upon the MTT[58] assay **Fig 3(a, b, c)**. The results showed that exposure to the various concentrations of FA-CisCCNPs formulation resulted in a dose and time-dependent inhibition of growth of B-16 cells, as depicted in Fig. 3a. This figure demonstrates FA-CCNPs concentration-dependent cytotoxicity, exhibiting potent inhibition of cell growth with IC_{50} value being 4830 µg/ml and 4841.35 µg/mL post 24hr and 48hr treatment, respectively. Then FA-CisCCNPs IC_{50} was evaluated to be 317.71 µg/ml and 141.11µg/ml.

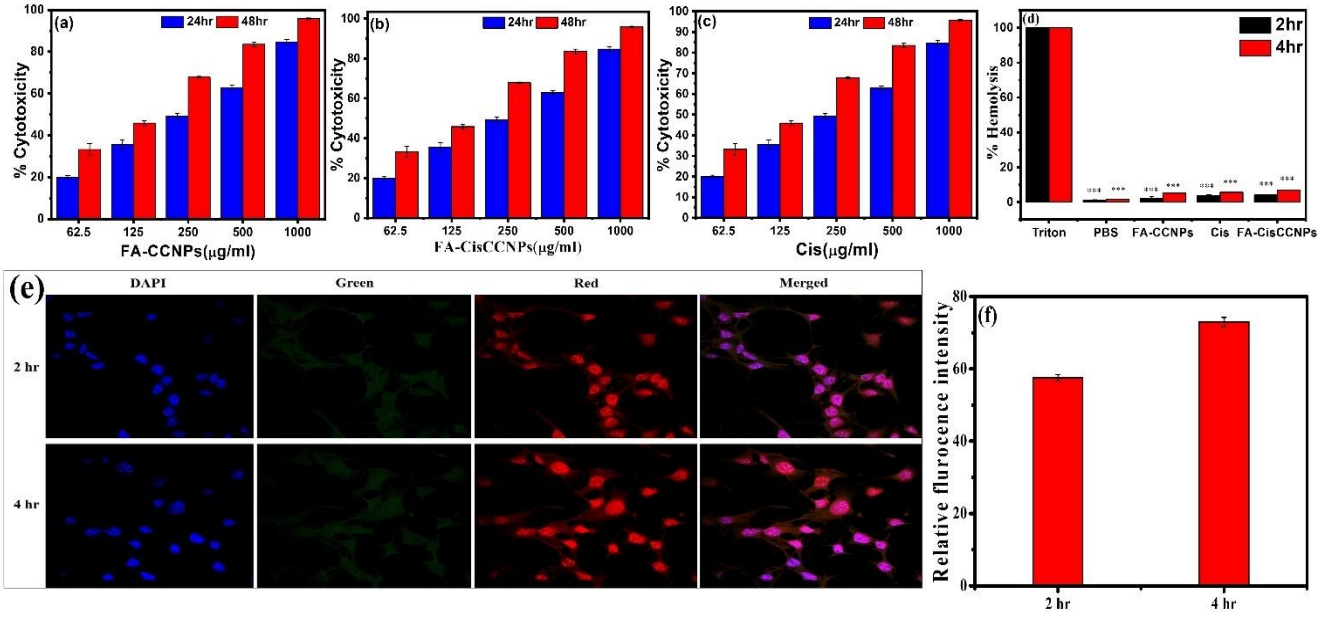

Figure 3 (a,b,c) Dose and 24 & 48 hr time dependant cytotoxicity of FA-CCNPs, Cis and FA-CisCCNPs in B-16 cell line (d) ex vivo hemolysis 2 hr and 4 hr post treatment with FA-CCNPs, Cis and FA-CisCCNPs and its comparison with positive (triton X-100) and negative (PBS) control. (e) Intracellular localization of FA-CCNPs in B-16 cells post 2hr and 4hr of incubation (60x). (f) Quantification of the uptake using mean fluorescence intensity of FA-CisCCNPs in individual B-16 cells. Data are represented as mean ± SD (n=3). *p<0.05; **p<0.01; ***p<0.001, where *denotes significant difference between control vs treated groups.

Further, it was also compared with the drug cis with IC50 values of 43.23 µg/mL and 29.20 µg/mL post-treatment at 24 hr and 48 hr. The IC_{50} of FA-CisCCNPs at each time point was lower than FA-CCNPs, showing the significant cytotoxicity of FA-CisCCNPs over FA-CCNPs[59].

View Article Online
DOI: 10.1039/D5NA00964B

3.3.2 Cellular uptake studies:

An essential consideration in determining nanotoxicity is the absorption of FA-CCNPs by cells. It is an effective and important consideration in the treatment of cancer due to the appropriate delivery of anti-cancer drugs to tumor cells. The cellular absorption of fluorescent FA-CCNPs and suspensions in this study was investigated in a time-dependent manner and was observed by confocal microscopy following two and four hours of incubation.

Fig 3 (e) shows that FA-CCNPs have a strong red fluorescence due to the presence of CQDs, which themselves have fluorescent nature. Here, the FA-CCNPs enter the B-16 cancer cell on exposure to the desired concentration of nano-formulation in RPMI medium at 37 °C for 2 and 4 hours. The green & red emission spectra for FA-CCNPs suggest internalisation of the FA-CCNPs. Cellular uptake was analysed using mean fluorescence intensity (ImageJ) **Fig 3 (f)** of FA-CCNPs that was increased over the course of incubation period, it depicted that B-16 cells were internalized with 60% of the FA-CCNPs post 2hr and 80% post 4hr. According to these results, FA-CCNPs is an effective anti-cancer drug carrier because of their small size, which allows them to pass through cell membranes and enter tumor cells. Targeted and operational cancer treatments may develop with the use of fluorescent FA-CCNPs as their cellular absorption may be seen and tracked.

3.3.3 Ex-vivo Hemolysis studies:

Hemolysis was performed to assess the NPs' biocompatibility **Fig 3 (d)**. This test is considered an easy and trustworthy method to evaluate a material's biocompatibility thus, confirming its usage for biomedical purposes[60]. Cis, FA-CCNPs & FA-CisCCNPs had shown extremely little hemolytic activity after 2 hours and 4 hours. Here, phosphate buffer saline (PBS) was used as the negative control and Triton X-100 as the positive control. NPs' interaction with red blood cells (RBCs) revealed a hemolysis percentage of less than 5%, which is considered a safe hemolytic ratio for biomaterials. This indicates that the FA-CisCCNPs damage to the RBCs was negligible. The findings suggest that the FA-CisCCNPs under investigation are biocompatible and could be a good fit for biological applications.

3.4 Tumour Regression Study

In-vivo anti-cancer studies were performed with B16-F10 melanoma cell line induced tumors in C57BL/6 mice model and its therapeutics with different samples and comparison with control

View Article Online
DOI: 10.1039/D5NA00964B

group. The therapeutic efficacy of placebo FA-CCNPs, FA-CisCCNPs, and Cis per se was evaluated by tumour regression analysis. The tumor mice were given intra-venous injections (IV) of different samples on alternate days for 21 days. The mice group receiving FA-CisCCNPs treatment showed significant tumor growth inhibition Fig4(a). In contrast, mice receiving treatment of placebo FA-CCNPs or Cis per se showed poor tumor growth inhibition. Not surprisingly, saline treated control mice group showed maximum tumor progression. The photographs of excised tumors and comparative analysis of body weight of control and different treatment groups are provided in Fig 4 (b,c), respectively. The analysis of tumor weight from the sacrificed mice further validated, significant tumor regression was seen in the FA-CisCCNPs treatment group Fig4(d). The anti-tumor efficacy of FA-CisCCNPs after intra-venous injection is possibly due to enhanced permeability and retention effect (EPR). In tumors, EPR effect is possible as the nano-drug delivery systems can accumulate based on their size as well as prolonged blood circulation time thus, reducing the tumor burden. The promising results in FA-CisCCNPs treated group in terms of less tumor volume are attributed to more accumulation of FA-CisCCNPs at tumor site which is the reason for initial burst release followed by sustained release of cisplatin from chitosan nanoparticles at tumor site. Therefore, the results demonstrated the therapeutic potential of chitosan as a biocompatible carrier for delivering cisplatin in melanoma treatment.

View Article Online
DOI: 10.1039/D5NA00964B

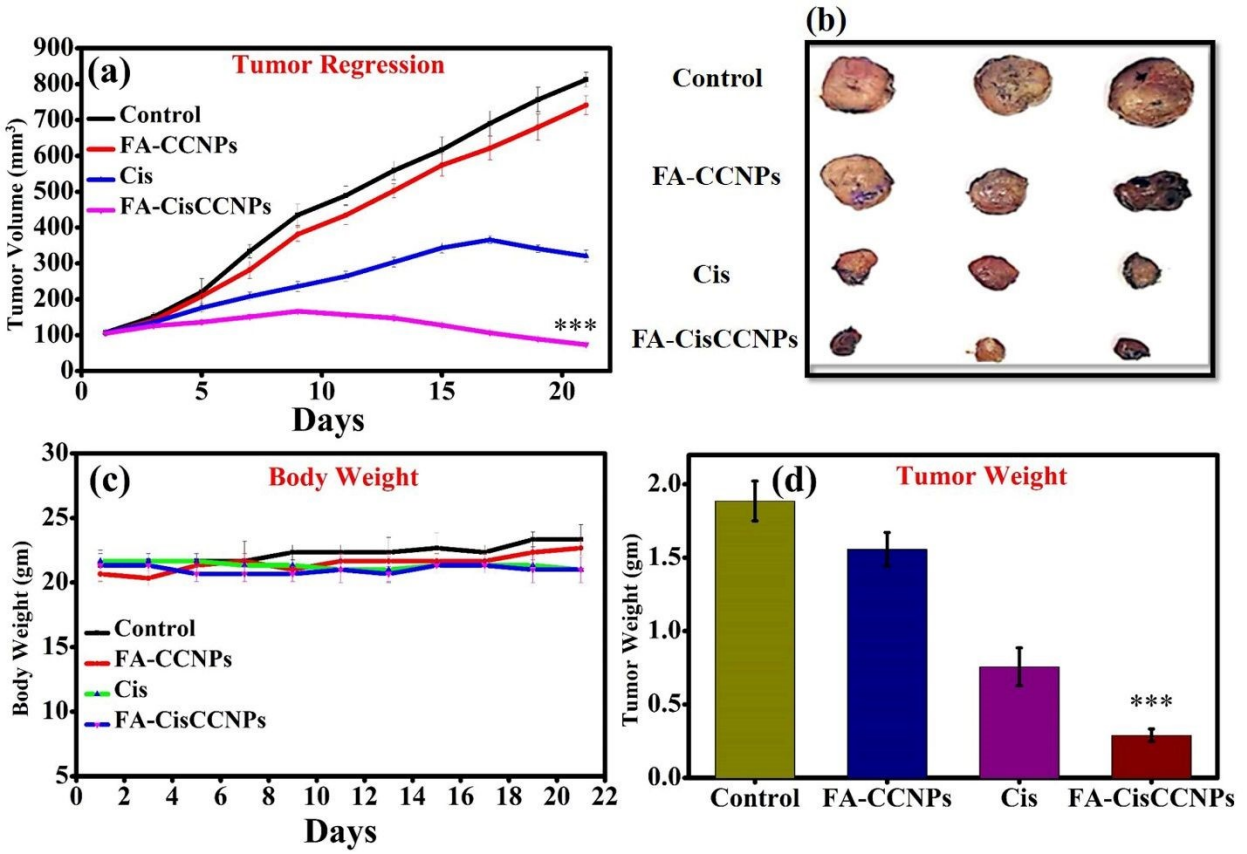

Figure 4: (a) Tumor regression curve after treatment; (b)Photographs of excised tumours on day 21; (c) Plot of Body weight of mice throughout the 21 days; (d) Weight of tumours excised on day 21. Data are represented as mean ± SD (n=3). *p<0.05; **p<0.01; ***p<0.001, where *denotes significant difference between control *vs* treated groups.

3.5 HISTOPATHOLOGICAL AND IMMUNOHISTOCHEMISTRY STUDIES

This structured approach not only elucidates the histopathological changes in the examined tissues but also contributes to a better understanding of the underlying mechanisms of treatment effects[61]. Tumor histology in the control, FA-CCNPs, and Cis treated groups shows dense tumor cell anatomy. In contrast, the FA-CisCCNPs-treated group exhibited a significantly reduced tumor cell volume, representative of an accelerated tumor regression mechanism, which is an anti-cancer effect caused by the sustained release of Cis from FA-CisCCNPs (Fig. 5). In the supplementary FigS4, Liver histology reveals the untreated control and cisplatin groups displayed histological

View Article Online
DOI: 10.1039/D5NA00964B

change in structure of the hepatocyte and central vein. The structural arrangement of portal veins, hepatic arteries, and bile ducts are disrupted. In the FA-CisCCNPs treated group, the disruption of the central vein was restructured, indicating that FA-CCNPs may have a protective effect against the toxicity caused by cisplatin. Kidney histology shows presence of normal glomerulus and tubule architecture, observed in both the control and cisplatin groups. In the FA-CisCCNPs treated group, glomeruli necrosis is indicated by nephrotoxicity. Conversely, the FA-CisCCNPs group mitigates potential nephrotoxicity, suggesting the protective effects of the FA-CCNPs nanoformulation. Spleen histopathological examination depicts a difference in the architecture of the spleen. In the control group, the spleen showed enlarged size. Subsequent treatment with FA-CisCCNPs resulted in a decrease in size, which was due to an upregulated filtration mechanism in spleenocytes and normalization post-treatment in the FA-CisCCNPs-treated groups Fig. S4). During tumor regression, increase in white pulp indicates immune activity, while the red pulp decreases as erythrocyte destruction diminishes, reflecting the body's efforts to eliminate tumor cells These findings support the therapeutic potential of FA-CisCCNPs in the treatment of melanoma cancer[62].

IHC analysis was done to assess the expression of Bcl-2 and p53 in tumor tissues, giving insight into the regulation of apoptosis and activation of tumor suppression[63]. This technique allows the visualization of protein expression within the tumor microenvironment. IHC analysis of tumor tissues for Bcl-2 and p53 revealed significant differences between the control and treatment groups[64]. The FA-CisCCNPs treated group showed evidently reduced Bcl-2 level, demonstrating the suppression of anti-apoptotic pathways, besides a significant increase in p53 expression reveals greater activation of tumor suppressor mechanisms Fig5. In contrast, control and FA-CCNPs groups showed increased Bcl-2 expression with minimal p53 level, suggesting limited apoptotic activity[65]. The Cis per se exhibited moderate changes in both BCL2 and p53 markers. The findings confirm that FA-CisCCNPs have better therapeutic efficacy by stimulating apoptosis via p53 activation and Bcl-2 downregulation, offering a promising strategy for melanoma treatment.

View Article Online
DOI: 10.1039/D5NA00964B

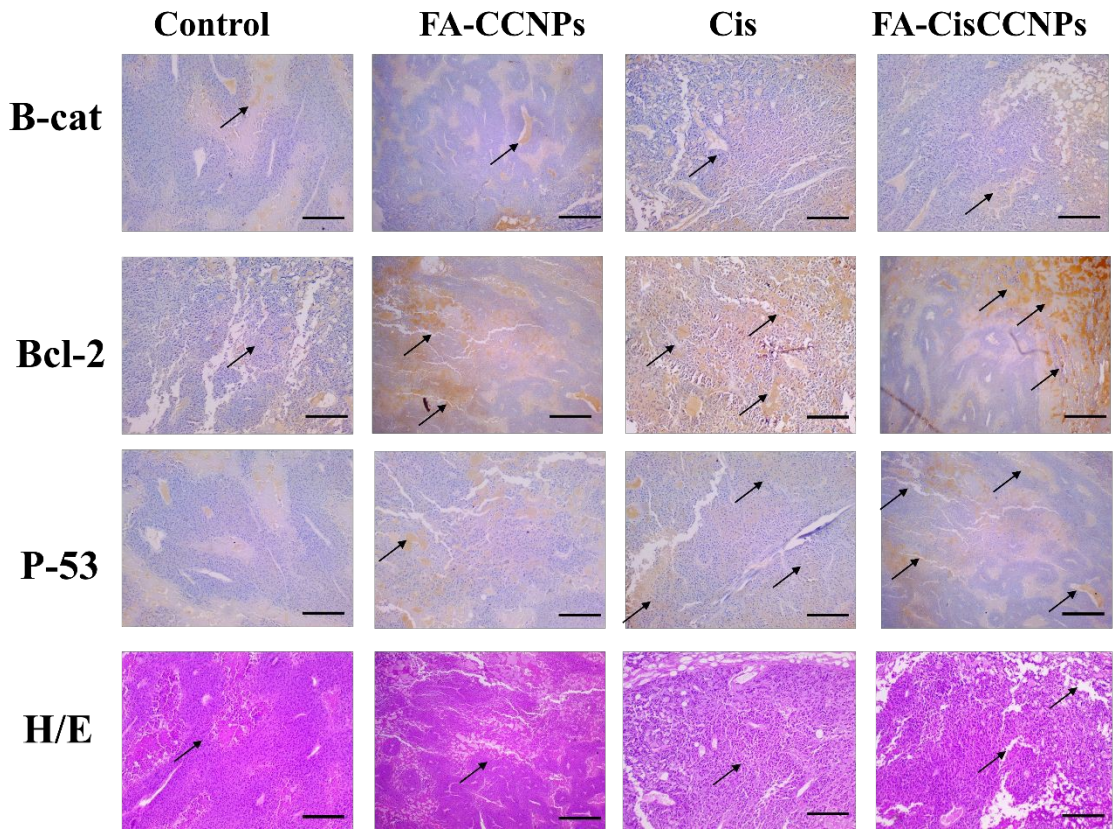

Figure 5: Immunohistochemistry analysis of B-cat, Bcl-2, p-53 expression and H&E tumor tissue image analysis in different treatment groups: Control, FA-CCNPs,Cis, and FA-CisCCNPs with scale bar = 200 µm, 10× magnification.

3.6. Biochemical Estimations

View Article Online
DOI: 10.1039/D5NA00964B

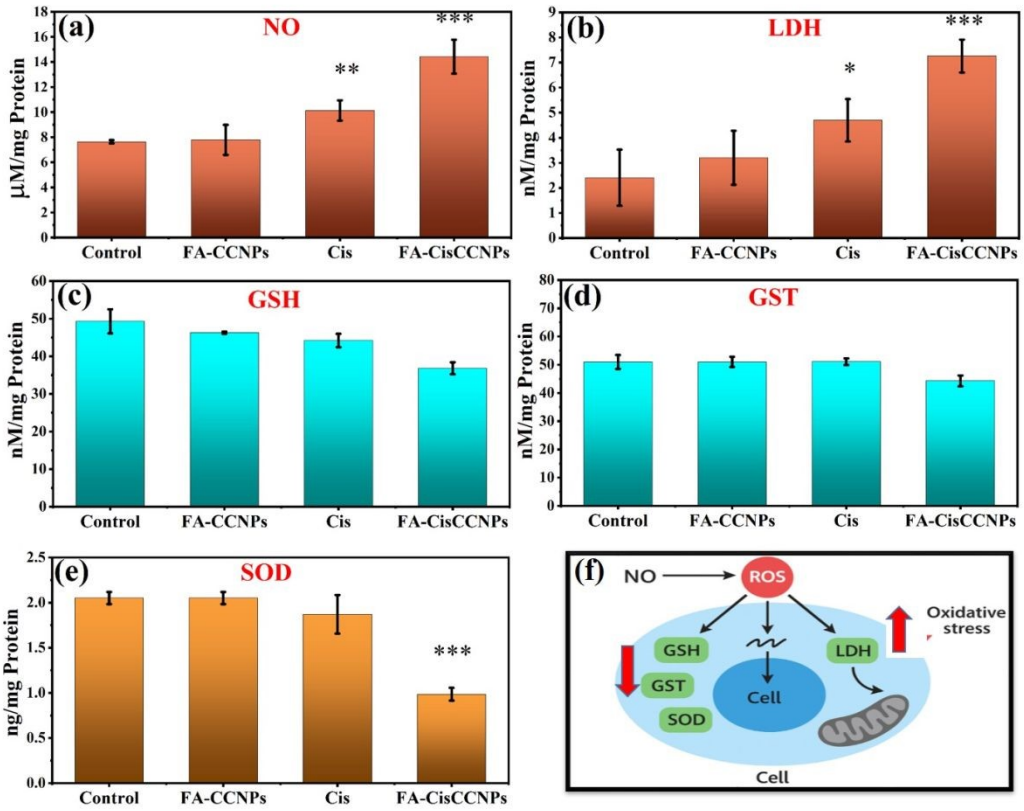

Figure 6(a-e) Estimation of NO, LDH, GSH, GST, SOD in tumor tissue homogenate of control, FA-CCNPs, Cis and FA-CisCCNPs after the end of experiment on day 21 (f) Schematic diagram of oxidative stress in tumor cells. Data are represented as mean ± SD (n=3). *p<0.05; **p<0.01; ***p<0.001, where *denotes significant difference between control *vs* treated groups.

Controlling ROS levels is important in cancer treatment because oxidative stress caused by excess ROS may help cancer develop[66]. Treatments like radiation and chemotherapy also generate ROS, which can fight tumors. Biomarkers like LDH and NO indicate oxidative stress in tumors. There are two types of NO synthase enzymes, iNOS and nNOS, that convert L-arginine into L-citrulline, producing nitric oxide (NO) in the tumor environment. This process requires oxygen and NADPH. iNOS is mainly used as an indicator to measure NO levels during inflammation surrounding tumors. Nitric oxide (NO) is one of the indicators for detecting the free radical generation. Studies

View Article Online
DOI: 10.1039/D5NA00964B

have shown the dual effects of NO in cancer. It is involved in both tumor progression and growth, but also exhibits tumoricidal effects[67]. Lowest NO level was observed in lung while highest amount was estimated in liver and kidney, shown in Fig S3(a). In tumor tissue FA-CisCCNPs group showed high NO level than the free Cis treated group. The levels of NO measured in tumor-bearing untreated control group is 7.63 ± 0.13 μM/mg of protien. In FA-CCNPs and Cis treated group, NO level was 7.79 ± 0.19 μM/mg and 10.13 ± 0.80 μM/mg protein and in FA-CisCCNPs groups it was estimated as 14.420 ±1.3461 μM/mg of protien, shown in Fig 6(a).

Lactate Dehydrogenase (LDH) is a marker for cellular leakage that provides information about possible cell membrane damage[68]. LDH levels were recorded in serum and the vital organs such as liver, kidney, spleen, heart, lung with untreated control and FA-CCNPs, Cis and FA-CisCCNPs group. Highest LDH release was observed in the liver, followed by heart, kidney. However Fig S3(b) shows Cis alone causes more LDH release than FA-CisCCNPs in all the organs and serum samples. In case of tumor tissue LDH level on its treatment with FA-CisCCNPs the LDH level was 7.25±0.65 nM/mg protein. In FA-CCNPs and Cis the estimated LDH level was 320±1.07 and 4.69±0.84 nM/mg protein, comparing all groups in FA-CisCCNPs it is high as compared to control group 2.4086 ±1.1191Fig 6(b).

Biochemical analysis included measuring several antioxidants from the glutathione family, such as GST, GSH, and SOD, in vital organs and serum on the 21st day of the study. This helped to better understand oxidative pathways in cancer and to evaluate how FA-CCNPs, Cis, and FA-CisCCNPs affected tumor reduction. Glutathione is an important anti-oxidant in the cellular system[69]. Therefore, to understand glutathione levels, we have measured both reduced and oxidized forms of glutathione. The levels of GSH were analysed in untreated control group and treated group FA-CCNPs, Cis and FA-CisCCNPs post 21 days of injection. The levels of GSH in FA-CisCCNPs treated group was compared to free Cis treated group in all the vital organs and serum and it was reduced as compare to control group. Highest amount of GSH was found in the spleen and lung and lowest in the kidney, shown in Fig S3(d).The level of GSH has marginally reduced in tumor tissue on treatment with FA-CisCCNPs, the estimated GSH level was 36.8161±1.5879 nM/mg protein when compared with control group 49.3128± 3.2016 nM/mg protein. In FA-CCNPs, Cis the GSH level was nM/mg protein 46.28±0.31 nM/mg and 44.21±1.77 nM/mg protein Fig 6(c). The Glutathione-S-transferases (GSTs) are a class of detoxification

View Article Online
DOI: 10.1039/D5NA00964B

enzymes which participates in the conjugation of glutathione to electrophilic compounds by thio-ester linkages[70]. The GST levels observed in the untreated control group were highest in spleen, lung, liver and lowest in lung. GST levels of FA-CisCCNPs treated group showed slightly elevated as compared to GST level of untreated control group in all the vital organs and serum,shown in FigS3(e). The level of GST in has reduced in FA-CisCCNPs treated tumor tissue 44.2521± 1.9527 when compared with control group 50.9589 ± 2.4589. In FA-CCNPs and Cis the GST level was 51.01±1.83 nM/mg protein and 51.06±1.15 nM/mg protein. Fig 6(d) .The superoxide dismutase activity was also measured in various experimental groups[71]. SOD levels were enhanced in FA-CisCCNPs treated group when compared with Cis, FA-CCNPs and untreated control group in all the vital organs and serum. Highest SOD level was found to be in the liver and lowest in lungs and serum, shown in FigS3(c). In tumor tissue FA-CCNPs, Cis the SOD level was 2.05 ± 0.06 ng/mg protein and 1.87 ± 0.21 ng/mg protein. A significant reduction was also seen in SOD level of FA-CisCCNPs treated tumor tissue which is 0.9853±0.705 ng/mg protein compare to control group 2.228 ±0.01252 ng/mg protein Fig 6(e). Data of oxidative stress of all vital organs including tumor tissue given in the supplementary file ST1

4. Discussion:

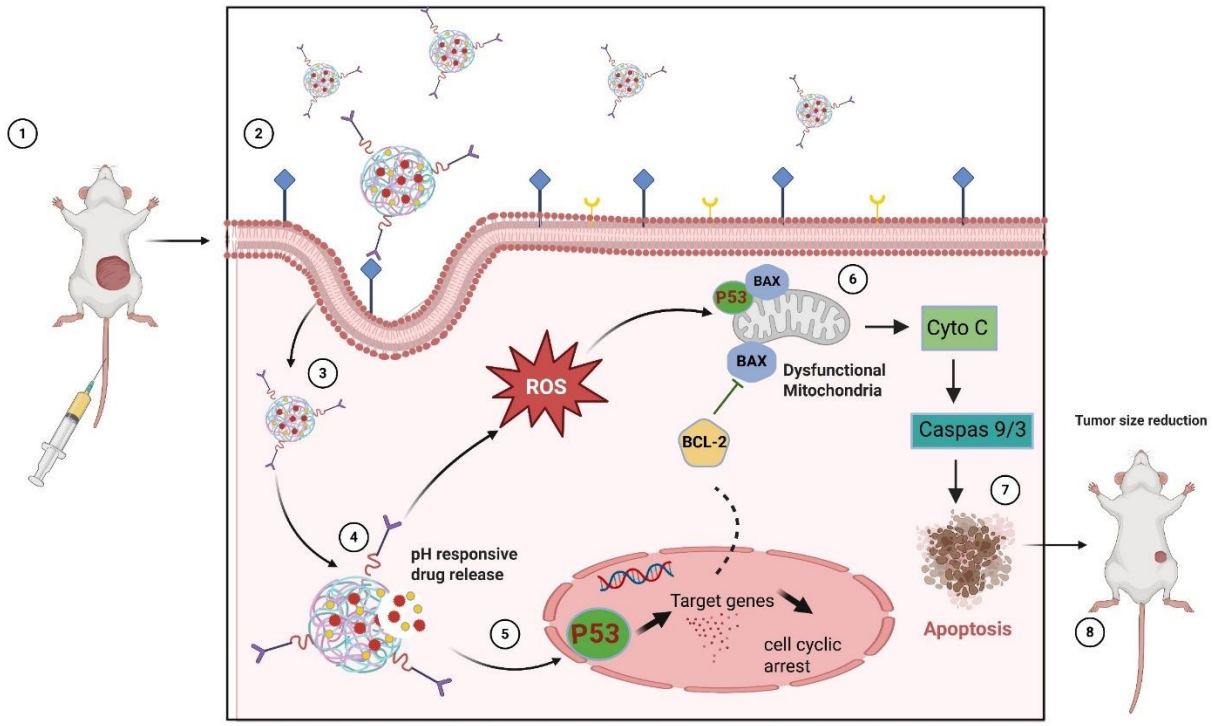

View Article Online
DOI: 10.1039/D5NA00964B

Fig 1(a-f) shows a comprehensive set of physicochemical characterizations confirming successful synthesis and integration of FA-CCNPs & FA-CisCCNPs. UV–Vis spectroscopy revealed distinct absorption peaks at 285 nm (CQDs), 290–320 nm (FA-CCNPs), and a reddened band at 370 nm. These peaks were caused by π–π* and n–π* electronic transitions due to aromatic conjugation and functional group interactions. The appearance of new peaks at 300 and 362 nm in FA-CisCCNPs showed that cisplatin was successfully loaded via ligand-to-metal charge transfer (LMCT). The photoluminescence (PL) spectra exhibited strong emission at 440 nm for CQDs when excited at 340 nm. Notably, the PL intensity was markedly reduced in FA-CisCCNPs, which can be attributed to surface passivation and quenching effects resulting from drug loading, although the residual fluorescence remains adequate for potential bioimaging applications. The nanoparticles were found to be cationic and colloidal stable, as shown by a zeta potential of +25.5 mV, indicative of excellent colloidal stability. DLS analysis showed that they had a mean hydrodynamic diameter of ~361 nm and a low polydispersity index (0.257), suggesting a uniform and monodisperse nanoparticle population. TEM images confirmed the formation of spherical, evenly distributed particles (~57 nm) with a smooth shape. SEM images further revealed the morphological differences, with FA-CCNPs exhibiting porous surfaces, while FA-CisCCNPs displayed a denser, smoother architecture, consistent with matrix compaction and drug entrapment. Fig2(a-g) highlights the FTIR analysis, which validated that the functional groups from CQDs, chitosan, folic acid, and cisplatin were successfully combined. Significant spectral shifts in the O–H/N–H, C=O, C–N, and P–O stretching vibrations confirmed successful chemical conjugation and strong intermolecular interactions among components. The XRD patterns showed the transition from crystalline cisplatin to a partly amorphous FA-CisCCNP structure, as evidenced by peak broadening and intensity reduction, implying uniform drug encapsulation within the polymeric framework. TGA research demonstrated improved thermal stability of the nanocomposite, with substantial residual mass at elevated temperatures attributable to the presence of inorganic platinum content, underscoring enhanced structural robustness suitable for biological applications. Collectively, these results affirm the successful fabrication of a structurally stable, biofunctionalized nanocomposite with high potential for targeted drug delivery and theranostic applications. Additionally, drug release kinetics were evaluated by fitting the experimental data, specifically the amount of drug released over time, to different mathematical models. These included the first-order release, zero-order release, Higuchi plot, and Korsmeyer-Peppas model.

View Article Online
DOI: 10.1039/D5NA00964B

These analyses confirmed that the nanoformulation exhibited an initial burst release under acidic tumor-mimicking conditions, followed by a sustained and controlled release extending up to 72 hours (Fig. S2). This biphasic release pattern reflects the structural integrity and pH-responsive behavior of the FA-CisCCNPs, supporting their suitability for targeted cancer therapy.

In vitro cytotoxicity study demonstrated that FA-CisCCNPs exhibits superior cytotoxicity compared to FA-CCNPs alone against B-16 melanoma cells, with significantly lower IC50 values (317.71 µg/mL and 141.11 µg/mL) at both 24 and 48 hours. Cis alone also showed potent inhibitory effects, confirming the enhanced efficacy of the FA-CisCCNPs formulation Fig3(a-c). The nanoparticles (Cis, FA-CCNPs, and FA-CisCCNPs) showed minimal hemolytic activity (<5%), indicating they are biocompatible and safe for biomedical use (Fig.3d). Cellular internalization experiments showed that fluorescent FA-CCNPs are effectively internalized by B-16 cancer cells, with uptake increasing from 60% at 2 hours to 80% at 4 hours. Their ability to enter cells suggests their potential as targeted drug delivery vehicles for melanoma treatment, and their fluorescence allows for tracking cellular absorption Fig3(e,f).

In-vivo experiments with melanoma-bearing mice showed that chitosan-cisplatin (FA-CisCCNPs) nanoparticles significantly slowed tumor growth over 21 days, performing better than both free cisplatin and placebo. The improved results are likely due to the nanoparticles accumulating passively at the tumor site via the EPR effect and releasing cisplatin gradually in the acidic tumor environment through lysosomal breakdown. These findings indicate that FA-CCNPs are a promising and safe delivery system for cisplatin in melanoma treatment. The study revealed that chitosan-cisplatin (FA-CisCCNPs) treatment significantly reduced tumor size and improved tissue health in melanoma-bearing mice Fig4(a-d).Fig 6 showing the understanding role of ROS in cancer, oxidative stress, caused by increased ROS or reduced antioxidant defenses, is linked to cancer development[72]. The interplay of antioxidants in melanoma cancer involves a complex balance between reactive oxygen species (ROS) and the body's defence mechanisms. In melanoma, elevated ROS levels can promote tumor growth, progression, and resistance to therapy by inducing genetic mutations and supporting cellular survival pathways[73]. To counteract oxidative stress, melanoma cells often upregulate antioxidant systems, such as glutathione (GSH), superoxide dismutase (SOD)[74], and enzymes like GST. This antioxidant response helps melanoma cells survive in a hostile, high-ROS environment and can contribute to resistance against

View Article Online
DOI: 10.1039/D5NA00964B

724 treatments like chemotherapy and radiotherapy. Understanding this delicate antioxidant-ROS
725 balance is crucial for developing therapies that can effectively target melanoma cells by
726 modulating oxidative stress pathways. The study revealed that FA-CisCCNPs treatment increased
727 oxidative stress in tumor tissue, as shown by higher NO and LDH levels and reduced antioxidants,
728 leading to cisplatin-induced ROS generation and effective tumor regression is seen and it also
729 improved tissue health in melanoma-bearing mice, showing protective effects on the liver, kidneys,
730 and spleen. Further Histological studies of tumor tissue along with various vital organ shows
731 restoration of tissue anatomy[75] and immunohistochemical analyses indicated that FA-CisCCNPs
732 enhances apoptosis by activating p-53[76] and suppressing Bcl-2[77] mediated BAX[78] inhibition in
733 tumor tissue, suggesting its potential role as an effective and safe melanoma therapy Fig5.
734

735 **5. Conclusion**

736 In this work we developed and evaluated folic acid-conjugated, cisplatin-loaded chitosan–carbon
737 quantum dot nanoparticles (FA-CisCCNPs) as a targeted nanotherapeutic system for melanoma
738 treatment. Folic acid was employed to facilitate receptor-mediated endocytosis into folate
739 receptor-overexpressing melanoma cells[79 80]. Comprehensive physicochemical characterization,
740 including electron microscopy, FTIR, XRD, TGA, and UV–Vis spectroscopy, confirmed the
741 structural integrity, efficient drug encapsulation, and thermal stability of the nanoformulation. In
742 vitro studies demonstrated significantly enhanced cytotoxicity of FA-CisCCNPs against B16
743 melanoma cells, reflected by a reduced IC50 compared to free cisplatin and nanoparticle controls.
744 Confocal imaging confirmed time-dependent intracellular uptake via folate-mediated
745 internalization, and hemolysis assays established the formulation's hemocompatibility. In vivo
746 evaluation in melanoma-bearing mice revealed pronounced tumor suppression in the FA-
747 CisCCNP-treated group, along with preserved tissue architecture and reduced systemic toxicity.
748 Histopathological analyses indicated improved liver, kidney, and spleen morphology, while
749 immunohistochemistry confirmed elevated p53 expression and suppressed Bcl-2, supporting
750 apoptosis induction. Additionally, FA-CisCCNPs modulated oxidative stress markers, suggesting
751 dual benefits of tumor regression and protection against cisplatin-induced damage.

View Article Online
DOI: 10.1039/D5NA00964B

This multifunctional, biocompatible nanocarrier offers a promising strategy for targeted melanoma therapy, addressing key limitations of conventional chemotherapy. Further exploration of pharmacokinetics and long-term safety may facilitate future clinical translation.

Ethical conduct of research

The authors state that they have obtained appropriate institutional review board approval for animal experimental investigations. under animal Ethical Committee of University of Delhi, India having registration number 1666/GO/Re/S/12/CPCSEA & Protocol number (DU/KR/IAEC/2023/13B)

6. Acknowledgement

SKS acknowledges his DST Inspire fellowship, MY acknowledges her CSIR senior research fellowship, PS acknowledges her UGC senior research fellowship.

7. Conflict of interest

The authors declare no competing financial interest.

8. References

1 M. Rady, I. Gomaa, N. Afifi and M. Abdel-Kader, Dermal delivery of Fe-chlorophyllin via ultradeformable nanovesicles for photodynamic therapy in melanoma animal model, *International Journal of Pharmaceutics*, 2018, **548**, 480–490.

2 R. A. Akasov, N. V. Sholina, D. A. Khochenkov, A. V. Alova, P. V. Gorelkin, A. S. Erofeev, A. N. Generalova and E. V. Khaydukov, Photodynamic therapy of melanoma by blue-light photoactivation of flavin mononucleotide, *Sci Rep*, 2019, **9**, 9679.

3 A. F. Moreira, C. F. Rodrigues, T. A. Jacinto, S. P. Miguel, E. C. Costa and I. J. Correia, Microneedle-based delivery devices for cancer therapy: A review, *Pharmacological Research*, 2019, **148**, 104438.

4 T.-A. Moo, R. Sanford, C. Dang and M. Morrow, Overview of Breast Cancer Therapy, *PET Clinics*, 2018, **13**, 339–354.

5 B. Biersack, Interactions between anticancer active platinum complexes and non-coding RNAs/microRNAs, *Non-coding RNA Research*, 2017, **2**, 1–17.

6 Mechanisms of Cisplatin Nephrotoxicity, https://www.mdpi.com/2072-6651/2/11/2490, (accessed 8 July 2025).

7 H. S. Oberoi, N. V. Nukolova, A. V. Kabanov and T. K. Bronich, Nanocarriers for delivery of platinum anticancer drugs, *Advanced Drug Delivery Reviews*, 2013, **65**, 1667–1685.

View Article Online
DOI: 10.1039/D5NA00964B

8 New Insights into Mechanisms of Cisplatin Resistance: From Tumor Cell to Microenvironment, https://www.mdpi.com/1422-0067/20/17/4136, (accessed 8 July 2025).

9 Full article: Recent progress in nanotechnology-based novel drug delivery systems in designing of cisplatin for cancer therapy: an overview, https://www.tandfonline.com/doi/full/10.1080/21691401.2019.1604535, (accessed 8 July 2025).

10 A. Atik, T. Günal, P. A. Bozkurt, S. N. Köse, B. Alp, C. Yandım, N. M. Kaleli, G. Kabay and G. Kaleli-Can, Characterization of cisplatin loaded hydrophilic glycol chitosan modified eumelanin nanoparticles for potential controlled-release application, *Journal of Drug Delivery Science and Technology*, 2023, **84**, 104440.

11 Advanced targeted drug delivery by bioengineered white blood cell-membrane camouflaged nanoparticulate delivery nanostructures - ScienceDirect, https://www.sciencedirect.com/science/article/abs/pii/S001393512301811X?via%3Dihub, (accessed 8 July 2025).

12 “Nanodecoys” - Future of drug delivery by encapsulating nanoparticles in natural cell membranes - ScienceDirect, https://www.sciencedirect.com/science/article/abs/pii/S0378517322003453?via%3Dihub, (accessed 8 July 2025).

13 A. Sheikh, S. Md, N. A. Alhakamy and P. Kesharwani, Recent development of aptamer conjugated chitosan nanoparticles as cancer therapeutics, *International Journal of Pharmaceutics*, 2022, **620**, 121751.

14 V. S. Madamsetty, S. Tavakol, S. Moghassemi, A. Dadashzadeh, J. D. Schneible, I. Fatemi, A. Shirvani, A. Zarrabi, F. Azedi, A. Dehshahri, A. Aghaei Afshar, K. Aghaabbasi, A. Pardakhty, R. Mohammadinejad and P. Kesharwani, Chitosan: A versatile bio-platform for breast cancer theranostics, *Journal of Controlled Release*, 2022, **341**, 733–752.

15 Chitosan: A Potential Biopolymer in Drug Delivery and Biomedical Applications, https://www.mdpi.com/1999-4923/15/4/1313, (accessed 9 July 2025).

16 Chitosan: A Natural Biopolymer with a Wide and Varied Range of Applications, https://www.mdpi.com/1420-3049/25/17/3981, (accessed 9 July 2025).

17 M. Prabaharan and J. F. Mano, Chitosan-Based Particles as Controlled Drug Delivery Systems, *Drug Delivery*, 2004, **12**, 41–57.

18 P. Kesharwani, K. Halwai, S. K. Jha, M. H. AL Mughram, S. S. Almujri, W. H. Almalki and A. Sahebkar, Folate-engineered chitosan nanoparticles: next-generation anticancer nanocarriers, *Molecular Cancer*, 2024, **23**, 244.

19 O. Young, N. Ngo, L. Lin, L. Stanbery, J. F. Creeden, D. Hamouda and J. Nemunaitis, Folate Receptor as a Biomarker and Therapeutic Target in Solid Tumors, *Current Problems in Cancer*, 2023, **47**, 100917.

View Article Online
DOI: 10.1039/D5NA00964B

819 20 Advances in targeting the folate receptor in the treatment/imaging of cancers - Chemical
820 Science (RSC Publishing), https://pubs.rsc.org/en/content/articlelanding/2018/sc/c7sc04004k, (accessed
821 8 July 2025).

822 21 S. K. Srivastava, R. Pratap, M. Yadav, M. Mishra, S. Chaudhary, R. Chawla, A. K. Verma and A. S.
823 Parmar, Biogenic synthesis of highly stable multifluorescent, multifaceted carbon quantum dots as dual
824 probe sensor for detection of heavy toxic metal ions – Fe3 + and As3+ in water and mouse fibroblast cell
825 line NIH-3T3, and for live in-vivo imaging in mice, *Colloids and Surfaces A: Physicochemical and*
826 *Engineering Aspects*, 2025, **723**, 137336.

827 22 R. Pratap, N. Hassan, M. Yadav, S. K. Srivastava, S. Chaudhary, A. K. Verma, J. Lahiri and A. S.
828 Parmar, Biogenic synthesis of dual-emission chlorophyll-rich carbon quantum dots for detection of toxic
829 heavy metal ions – Hg(II) and As(III) in water and mouse fibroblast cell line NIH-3T3, *Environ. Sci.: Nano*,
830 2024, **11**, 1636–1653.

831 23 Biogenic Synthesis of Gold Nanoparticles Using Dual Extract of Tulsi–Vinca for Breast Cancer
832 Tumor Regression in Mice: Nanomedicine: Vol 18, No 26,
833 https://www.tandfonline.com/doi/abs/10.2217/nnm-2023-0208, (accessed 8 July 2025).

834 24 M. Zoghi, M. Pourmadadi, F. Yazdian, M. N. Nigjeh, H. Rashedi and R. Sahraeian, Synthesis and
835 characterization of chitosan/carbon quantum dots/Fe2O3 nanocomposite comprising curcumin for
836 targeted drug delivery in breast cancer therapy, *International Journal of Biological Macromolecules*,
837 2023, **249**, 125788.

838 25 C. C. Skinner, E. L. McMichael, A. C. Jaime-Ramirez, Z. B. Abrams, R. J. Lee and W. E. Carson,
839 Folate-conjugated immunoglobulin targets melanoma tumor cells for NK cell effector functions,
840 *Melanoma Res*, 2016, **26**, 329–337.

841 26 Biogenic synthesis of highly stable multifluorescent, multifaceted carbon quantum dots as dual
842 probe sensor for detection of heavy toxic metal ions – Fe3 + and As3+ in water and mouse fibroblast cell
843 line NIH-3T3, and for live in-vivo imaging in mice - ScienceDirect,
844 https://www.sciencedirect.com/science/article/pii/S0927775725012397, (accessed 10 July 2025).

845 27 Interests of chitosan nanoparticles ionically cross-linked with tripolyphosphate for biomedical
846 applications,
847 https://www.researchgate.net/publication/304779177_Interests_of_chitosan_nanoparticles_ionically_c
848 ross-linked_with_tripolyphosphate_for_biomedical_applications, (accessed 10 July 2025).

849 28 5-Fluorouracil-Loaded Folic-Acid-Fabricated Chitosan Nanoparticles for Site-Targeted Drug
850 Delivery Cargo, https://www.mdpi.com/2073-4360/14/10/2010, (accessed 11 July 2025).

851 29 M. Lazaridou, E. Christodoulou, M. Nerantzaki, M. Kostoglou, D. A. Lambropoulou, A. Katsarou,
852 K. Pantopoulos and D. N. Bikiaris, Formulation and In-Vitro Characterization of Chitosan-Nanoparticles
853 Loaded with the Iron Chelator Deferoxamine Mesylate (DFO), *Pharmaceutics*, 2020, **12**, 238.

854 30 S. Wijayawardana, C. Thambiliyagodage and M. Jayanetti, Kinetic study of *in vitro* release of
855 curcumin from chitosan biopolymer and the evaluation of biological efficacy, *Arabian Journal of*
856 *Chemistry*, 2024, **17**, 105896.

View Article Online
DOI: 10.1039/D5NA00964B

857 31 M. Ferrari, M. C. Fornasiero and A. M. Isetta, MTT colorimetric assay for testing macrophage
858 cytotoxic activity in vitro, *J Immunol Methods*, 1990, **131**, 165–172.

859 32 K. Naik, P. Singh, M. Yadav, S. K. Srivastava, S. Tripathi, R. Ranjan, P. Dhar, A. K. Verma, S.
860 Chaudhary and A. S. Parmar, 3D printable, injectable amyloid-based composite hydrogel of bovine
861 serum albumin and aloe vera for rapid diabetic wound healing, *J. Mater. Chem. B*, 2023, **11**, 8142–8158.

862 33 Biogenic Synthesis of Gold Nanoparticles Using Dual Extract of Tulsi–Vinca for Breast Cancer
863 Tumor Regression in Mice: Nanomedicine: Vol 18, No 26,
864 https://www.tandfonline.com/doi/abs/10.2217/nnm-2023-0208, (accessed 29 December 2025).

865 34 S. Garg, S. Tripathi, S. Agrawal, V. Tiwari and A. S. Parmar, Nanocomposite conductive r(GO/BSA)
866 hydrogel as an effective dressing for rapid chronic diabetic wound healing, *Colloids and Surfaces A:*
867 *Physicochemical and Engineering Aspects*, 2025, **705**, 135553.

868 35 W. W. Overwijk and N. P. Restifo, B16 as a Mouse Model for Human Melanoma, *Curr Protoc*
869 *Immunol*, 2001, **CHAPTER**, Unit-20.1.

870 36 Hydrothermal synthesis and characterization of carbon quantum dots from paneer whey and
871 evaluation of their in-vitro safety, anti-oxidant and antagonistic properties | Request PDF,
872 https://www.researchgate.net/publication/392132621_Hydrothermal_synthesis_and_characterization_
873 of_carbon_quantum_dots_from_paneer_whey_and_evaluation_of_their_in-vitro_safety_anti-
874 oxidant_and_antagonistic_properties, (accessed 12 July 2025).

875 37 Preparation and In Vitro Characterization of Chitosan Nanoparticles and Their Broad-Spectrum
876 Antifungal Action Compared to Antibacterial Activities against Phytopathogens of Tomato,
877 https://www.mdpi.com/2073-4395/9/1/21, (accessed 12 July 2025).

878 38 UV/Vis absorption spectroelectrochemistry of folic acid | Journal of Solid State Electrochemistry,
879 https://link.springer.com/article/10.1007/s10008-021-05026-5, (accessed 24 December 2025).

880 39 Tripolyphosphate-Driven Synthesis of Ag3PO4-Decorated Chitosan Nanoparticles for Enhanced
881 Antimicrobial Activity, https://www.researchgate.net/publication/394887436_Tripolyphosphate-
882 Driven_Synthesis_of_Ag3PO4-
883 Decorated_Chitosan_Nanoparticles_for_Enhanced_Antimicrobial_Activity, (accessed 24 December
884 2025).

885 40 pH sensitive and controlled release system based on cellulose nanofibers-poly vinyl alcohol
886 hydrogels for cisplatin delivery,
887 https://www.researchgate.net/publication/315925523_pH_sensitive_and_controlled_release_system_
888 based_on_cellulose_nanofibers-poly_vinyl_alcohol_hydrogels_for_cisplatin_delivery, (accessed 24
889 December 2025).

890 41 S. A. Abass, A. A. Elgazar, S. S. El-kholy, A. I. El-Refaiy, R. A. Nawaya, M. A. Bhat, F. A. Farrag, A.
891 Hamdi, M. Balaha and M. A. El-Magd, Unraveling the Nephroprotective Potential of Papaverine against
892 Cisplatin Toxicity through Mitigating Oxidative Stress and Inflammation: Insights from In Silico, In Vitro,
893 and In Vivo Investigations, *Molecules*, 2024, **29**, 1927.

View Article Online
DOI: 10.1039/D5NA00964B

894 42 Development and characterization of hydrogels based on natural polysaccharides: Policaju and
895 chitosan - ScienceDirect,
896 https://www.sciencedirect.com/science/article/pii/S0928493114002859?via%3Dihub, (accessed 10 July
897 2025).

898 43 H. Katas, M. A. G. Raja and K. L. Lam, Development of Chitosan Nanoparticles as a Stable Drug
899 Delivery System for Protein/siRNA, *International Journal of Biomaterials*, 2013, **2013**, 146320.

900 44 S. K. Srivastava, R. Pratap, M. Yadav, M. Mishra, S. Chaudhary, R. Chawla, A. K. Verma and A. S.
901 Parmar, Biogenic synthesis of highly stable multifluorescent, multifaceted carbon quantum dots as dual
902 probe sensor for detection of heavy toxic metal ions – Fe3 + and As3+ in water and mouse fibroblast cell
903 line NIH-3T3, and for live in-vivo imaging in mice, *Colloids and Surfaces A: Physicochemical and*
904 *Engineering Aspects*, 2025, **723**, 137336.

905 45 Release of Anticancer Drug 5-Fluorouracil from Different Ionically Crosslinked Alginate Beads,
906 https://www.scirp.org/journal/paperinformation?paperid=23732, (accessed 10 July 2025).

907 46 Caprylate-Conjugated Cisplatin for the Development of Novel Liposomal Formulation | AAPS
908 PharmSciTech, https://link.springer.com/article/10.1208/s12249-014-0106-y, (accessed 10 July 2025).

909 47 Does the Use of Chitosan Contribute to Oxalate Kidney Stone Formation?,
910 https://www.mdpi.com/1660-3397/13/1/141, (accessed 10 July 2025).

911 48 Y. Tsong, T. Hammerstrom and J. J. Chen, Multipoint dissolution specification and acceptance
912 sampling rule based on profile modeling and principal component analysis, *Journal of Biopharmaceutical*
913 *Statistics*, 1997, **7**, 423–439.

914 49 M. H. Sultan, S. S. Moni, O. A. Madkhali, M. A. Bakkari, S. Alshahrani, S. S. Alqahtani, N. A.
915 Alhakamy, S. Mohan, M. Ghazwani, H. A. Bukhary, Y. Almoshari, A. Salawi and M. Alshamrani,
916 Characterization of cisplatin-loaded chitosan nanoparticles and rituximab-linked surfaces as target-
917 specific injectable nano-formulations for combating cancer, *Sci Rep*, 2022, **12**, 468.

918 50 M. Lazaridou, E. Christodoulou, M. Nerantzaki, M. Kostoglou, D. A. Lambropoulou, A. Katsarou,
919 K. Pantopoulos and D. N. Bikiaris, Formulation and In-Vitro Characterization of Chitosan-Nanoparticles
920 Loaded with the Iron Chelator Deferoxamine Mesylate (DFO), *Pharmaceutics*, 2020, **12**, 238.

921 51 A. Sethi, M. Ahmad, T. Huma, I. Khalid and I. Ahmad, Evaluation of Low Molecular Weight Cross
922 Linked Chitosan Nanoparticles, to Enhance the Bioavailability of 5-Flourouracil, *Dose Response*, 2021, **19**,
923 15593258211025353.

924 52 N. E.-A. El-Naggar, A. M. Shiha, H. Mahrous and A. B. A. Mohammed, Green synthesis of chitosan
925 nanoparticles, optimization, characterization and antibacterial efficacy against multi drug resistant
926 biofilm-forming Acinetobacter baumannii, *Sci Rep*, 2022, **12**, 19869.

927 53 S. W. Ali, S. Rajendran and M. Joshi, Synthesis and characterization of chitosan and silver loaded
928 chitosan nanoparticles for bioactive polyester, *Carbohydrate Polymers*, 2011, **83**, 438–446.

929 54 M. Chen, T. Runge, L. Wang, R. Li, J. Feng, X.-L. Shu and Q.-S. Shi, Hydrogen bonding impact on
930 chitosan plasticization, *Carbohydrate Polymers*, 2018, **200**, 115–121.

View Article Online
DOI: 10.1039/D5NA00964B

55 M. Y. Kim and J. Lee, Chitosan fibrous 3D networks prepared by freeze drying, *Carbohydrate Polymers*, 2011, **84**, 1329–1336.

56 S. A. Kahdestani, M. H. Shahriari and M. Abdouss, Synthesis and characterization of chitosan nanoparticles containing teicoplanin using sol–gel, *Polym. Bull.*, 2021, **78**, 1133–1148.

57 The Potential Cytotoxic Activity Enhancement of α-Mangostin in Chitosan-Kappa Carrageenan-Loaded Nanoparticle against MCF-7 Cell Line, https://www.mdpi.com/2073-4360/13/11/1681, (accessed 12 July 2025).

58 Skin Adhesive 3D-Printable BSA-Amyloid/Cellulose Hybrid Hydrogel Film for Rapid Wound Healing and Skin Regeneration with Enhanced Antioxidant and Anti-Inflammatory Properties | ACS Applied Bio Materials, https://pubs.acs.org/doi/full/10.1021/acsabm.5c01216, (accessed 29 December 2025).

59 Bioactive hyaluronic acid – Protein based amyloidogenic hydrogel dressing for rapid diabetic wound healing via enhanced angiogenesis and anti-inflammation - ScienceDirect, https://www.sciencedirect.com/science/article/pii/S2352492825020720, (accessed 29 December 2025).

60 S. Tripathi, N. K. Mishra, S. Agarwal, A. Upadhyay, S. Chaudhary, S. Mukherjee, S. K. Yadav and A. S. Parmar, Nature-inspired dermal barrier: Tunable biofunctional BSA-fenugreek films and spreadable soft hydrogel for skin photoprotection and healing, *Colloids and Surfaces B: Biointerfaces*, 2026, **259**, 115358.

61 C.-H. Weng, C.-S. Wu, J.-C. Wu, M.-L. Kung, M.-H. Wu and M.-H. Tai, Cisplatin-Induced Giant Cells Formation Is Involved in Chemoresistance of Melanoma Cells, *Int J Mol Sci*, 2020, **21**, 7892.

62 X. Zhang, G. Zheng, Z. Zhou, M. Zhu and S. Tang, Co-delivery of siRNA and cisplatin via electrospun Nanofibrous membranes for synergistic treatment of malignant melanoma, *Heliyon*, 2024, **10**, e37517.

63 A. R. Goloudina, K. Tanoue, A. Hammann, E. Fourmaux, X. Le Guezennec, D. V. Bulavin, S. J. Mazur, E. Appella, C. Garrido and O. N. Demidov, Wip1 promotes RUNX2-dependent apoptosis in p53-negative tumors and protects normal tissues during treatment with anticancer agents, *Proc Natl Acad Sci U S A*, 2012, **109**, E68-75.

64 L. Galluzzi, I. Vitale, J. Michels, C. Brenner, G. Szabadkai, A. Harel-Bellan, M. Castedo and G. Kroemer, Systems biology of cisplatin resistance: past, present and future, *Cell Death Dis*, 2014, **5**, e1257.

65 T. Sperka, J. Wang and K. L. Rudolph, DNA damage checkpoints in stem cells, ageing and cancer, *Nat Rev Mol Cell Biol*, 2012, **13**, 579–590.

66 Oxidative Stress in Melanoma: Beneficial Antioxidant and Pro-Oxidant Therapeutic Strategies - PMC, https://pmc.ncbi.nlm.nih.gov/articles/PMC10252072/, (accessed 24 December 2025).

67 S. S. Beevi, M. H. Rasheed and A. Geetha, Evidence of oxidative and nitrosative stress in patients with cervical squamous cell carcinoma, *Clin Chim Acta*, 2007, **375**, 119–123.

View Article Online
DOI: 10.1039/D5NA00964B

68 Preparation, characterization, and antibacterial activity of diclofenac-loaded chitosan nanoparticles, https://www.researchgate.net/publication/327292125_Preparation_characterization_and_antibacterial_activity_of_diclofenac-loaded_chitosan_nanoparticles, (accessed 10 July 2025).

69 O. W. Griffith, Determination of glutathione and glutathione disulfide using glutathione reductase and 2-vinylpyridine, *Anal Biochem*, 1980, **106**, 207–212.

70 W. H. Habig, M. J. Pabst and W. B. Jakoby, Glutathione S-transferases. The first enzymatic step in mercapturic acid formation, *J Biol Chem*, 1974, **249**, 7130–7139.

71 Y. Hu, D. G. Rosen, Y. Zhou, L. Feng, G. Yang, J. Liu and P. Huang, Mitochondrial manganese-superoxide dismutase expression in ovarian cancer: role in cell proliferation and response to oxidative stress, *J Biol Chem*, 2005, **280**, 39485–39492.

72 M. S. K. Naidu, A. N. Suryakar, S. C. Swami, R. V. Katkam and K. M. Kumbar, Oxidative stress and antioxidant status in cervical cancer patients, *Indian J Clin Biochem*, 2007, **22**, 140–144.

73 T. C. Hour, J. Chen, C. Y. Huang, J. Y. Guan, S. H. Lu, C. Y. Hsieh and Y. S. Pu, Characterization of chemoresistance mechanisms in a series of cisplatin-resistant transitional carcinoma cell lines, *Anticancer Res*, 2000, **20**, 3221–3225.

74 N. Taniguchi, M. Ishikawa, T. Kawaguchi, J. Fujii, K. Suzuki and T. Nakata, Expression of Mn-superoxide dismutase in carcinogenesis, *Tohoku J Exp Med*, 1992, **168**, 105–111.

75 J. G. Hengstler, H. Pilch, M. Schmidt, H. Dahlenburg, J. Sagemüller, I. Schiffer, F. Oesch, P. G. Knapstein, B. Kaina and B. Tanner, Metallothionein expression in ovarian cancer in relation to histopathological parameters and molecular markers of prognosis, *Int J Cancer*, 2001, **95**, 121–127.

76 Inhibition of Chk1 Kills Tetraploid Tumor Cells through a p53-Dependent Pathway | PLOS One, https://journals.plos.org/plosone/article?id=10.1371/journal.pone.0001337, (accessed 10 July 2025).

77 M. Sakamoto, A. Kondo, K. Kawasaki, T. Goto, H. Sakamoto, K. Miyake, Y. Koyamatsu, T. Akiya, H. Iwabuchi, T. Muroya, K. Ochiai, T. Tanaka, Y. Kikuchi and Y. Tenjin, Analysis of gene expression profiles associated with cisplatin resistance in human ovarian cancer cell lines and tissues using cDNA microarray, *Hum Cell*, 2001, **14**, 305–315.

78 N. Tajeddine, L. Galluzzi, O. Kepp, E. Hangen, E. Morselli, L. Senovilla, N. Araujo, G. Pinna, N. Larochette, N. Zamzami, N. Modjtahedi, A. Harel-Bellan and G. Kroemer, Hierarchical involvement of Bak, VDAC1 and Bax in cisplatin-induced cell death, *Oncogene*, 2008, **27**, 4221–4232.

79 E. Roger, S. Kalscheuer, A. Kirtane, B. R. Guru, A. E. Grill, J. Whittum-Hudson and J. Panyam, Folic acid-Functionalized Nanoparticles for Enhanced Oral Drug Delivery, *Mol Pharm*, 2012, **9**, 2103–2110.

80 Recent Advances in Nanoparticle-Based Cancer Drug and Gene Delivery - PMC, https://pmc.ncbi.nlm.nih.gov/articles/PMC6550462/, (accessed 11 February 2026).

View Article Online
DOI: 10.1039/D5NA00964B

Data availability statement

The data supporting this article have been included as part of the supplementary information (SI). Supplementary information: details of synthesis methods, *etc*. Table ST1; Fig. S1–S4.